The Astrophysical Journal, 928:138 (21pp), 2022 April 1 https://doi.org/10.3847/1538-4357/ac562d

Unveiling the Nature of SN 2011fh: A Young and Massive Star Gives Rise to a Luminous SN 2009ip−like Event

Thallis Pessi[1], Jose L. Prieto[1,2], Berto Monard[3], Christopher S. Kochanek[4,5], Greg Bock[6], Andrew J. Drake[7], Ori D. Fox[8], Stuart Parker[9], and Heloise F. Stevance[10]
[1] Núcleo de Astronomía, Universidad Diego Portales, Av. Ejército 441, Santiago, Chile; thallis.pessi@mail.udp.cl
[2] Millennium Institute of Astrophysics, Santiago, Chile
[3] Klein Karoo Observatory, Calitzdorp, South Africa
[4] Department of Astronomy, The Ohio State University, 140 West 18th Avenue, Columbus, OH 43210, USA
[5] Center for Cosmology and Astroparticle Physics, The Ohio State University, 191 W. Woodruff Avenue, Columbus, OH 43210, USA
[6] Runaway Bay, Gold Coast, Queensland, Australia
[7] Division of Physics, Mathematics, and Astronomy, California Institute of Technology, Pasadena, CA 91125, USA
[8] Space Telescope Science Institute, 3700 San Martin Drive, Baltimore, MD 21218, USA
[9] Parkdale Observatory, 225 Warren Road, RDl Oxford, Canterbury 7495, New Zealand
[10] Department of Physics, The University of Auckland, Private Bag 92019, Auckland, New Zealand
Received 2021 October 14; revised 2022 January 3; accepted 2022 January 16; published 2022 April 4

Abstract

In recent years, many Type IIn supernovae have been found to share striking similarities with the peculiar SN 2009ip, whose true nature is still under debate. Here, we present 10 yr of observations of SN 2011fh, an interacting transient with spectroscopic and photometric similarities to SN 2009ip. SN 2011fh had an $M_r \sim -16$ mag brightening event, followed by a brighter $M_r \sim -18$ mag luminous outburst in 2011 August. The spectra of SN 2011fh are dominated by narrow to intermediate Balmer emission lines throughout its evolution, with P Cygni profiles indicating fast-moving material at $\sim$6400 km s^{-1}. HST/WFC3 observations from 2016 October revealed a bright source with $M_{\rm F814W} \approx -13.3$ mag, indicating that we are seeing the ongoing interaction of the ejecta with the circumstellar material or that the star might be going through an eruptive phase five years after the luminous outburst of 2011. Using HST photometry of the stellar cluster around SN 2011fh, we estimated an age of $\sim$4.5 Myr for the progenitor, which implies a stellar mass of $\sim$60 $M_\odot$, using single-star evolution models, or a mass range of 35–80 $M_\odot$, considering a binary system. We also show that the progenitor of SN 2011fh exceeded the classical Eddington limit by a large factor in the months preceding the luminous outburst of 2011, suggesting strong super-Eddington winds as a possible mechanism for the observed mass loss. These findings favor an energetic outburst in a young and massive star, possibly a luminous blue variable.

Unified Astronomy Thesaurus concepts: Supernovae (1668); Stellar mass loss (1613); Massive stars (732); Transient sources (1851)

1. Introduction

Most stars with a zero-age main-sequence (ZAMS) mass higher than 8 $M_\odot$ are thought to end their lives as a core-collapse supernova (CCSN). An important fraction of these explosions happen inside a very dense environment, formed by the material ejected by the star in its previous mass-loss history. If the circumstellar material (CSM) is sufficiently dense and dominated by hydrogen, hydrogen emission lines with multiple velocity components appear, leading to a Type IIn supernova (SN; Schlegel 1990; Filippenko 1997; Ransome et al. 2021). If, on the other hand, the CSM is helium rich, a Type Ibn SN is observed (Pastorello et al. 2007, 2008). Recently, Type Icn SNe have been discovered, with narrow C and O lines, and no H and He lines (Fraser et al. 2021; Gal-Yam et al. 2021).

These events are sometimes referred to as interacting SNe because the characteristic emission lines in their spectra come from the ionization of the CSM by emission from the SN shock (Smith 2017; Fraser 2020). Other observational properties of these transients include a relatively blue continuum, very diverse and prolonged light curves (Taddia et al. 2015; Nyholm et al. 2020), and, for a fraction of interacting SNe, enhanced X-ray (Fox et al. 2000; Chandra et al. 2012a, 2012b; Katsuda et al. 2014) or radio emission (van Dyk et al. 1993; Pooley et al. 2002; Williams et al. 2002; Chandra et al. 2009).

The fact that we observe interacting SNe indicates that intense mass-loss activity can occur in the years preceding the collapse of the progenitor star, and we still do not have a good physical understanding of the mechanisms involved (see the review by Smith 2014). Standard stellar evolution models do not account for the amount of mass loss needed to explain these transients, limiting our understanding of their progenitors (Langer 2012). In fact, direct observations of the progenitor stars of Type IIn/Ibn SNe have been elusive, with only a few being confirmed (Gal-Yam et al. 2007; Gal-Yam & Leonard 2009; Smith et al. 2010, 2011; Foley et al. 2011).

The progenitors of interacting SNe can be diverse, which is highlighted by the extreme diversity in their observational properties (Taddia et al. 2015). The progenitor of the Type IIn SN 2005gl was a massive luminous blue variable (LBV)-like star (Gal-Yam & Leonard 2009), so at least some of these events are generated by LBV-like massive stars. Analysis of the environments of these explosions, however, show that interacting SNe happen in very similar locations to Type II SNe (Anderson et al. 2012; Kangas et al. 2017), indicating that they

might have overlapping mass ranges and are not confined to very massive stars.

Some massive stars can go through very unstable mass-loss phases, ejecting large amounts of matter in energetic eruptions and explosions (Smith 2014). One well-known example is the massive Galactic LBV Eta Carinae, which went through a major eruption event (the Great Eruption) in the 19th century, reaching an absolute magnitude of $M_V \sim -14$ and with properties similar to Type IIn SNe (Rest et al. 2012; Prieto et al. 2014; Smith et al. 2018a, 2018b). Estimates show that the star produced $\sim 10^{50}$ ergs of kinetic energy and ejected 10–20 $M_\odot$ of material (Smith et al. 2003; Smith 2006). The main mechanism that caused the Great Eruption of Eta Carinae is still under debate, although recent observations of its light echoes point to a possible merger in a triple system (Smith et al. 2018a; Hirai et al. 2021).

Some of these giant stellar eruptions happen inside a very dense medium and produce spectroscopically and photometrically similar transients to interacting SNe. Although being a nonterminal event, in the sense that the progenitor star is still alive afterwards, these outbursts also interact with the CSM. Because of these similarities, some of these outbursts are mistakenly classified as SNe, originating the term "supernova impostors." A famous impostor associated with a massive star progenitor is SN 1997bs, which had a peak at $M_V \simeq M_R \simeq -14$, a very slow decline in its light curve, and a spectrum dominated by strong narrow Hα in emission (Van Dyk et al. 2000), although there is presently no evidence that the star survived (Adams & Kochanek 2015). Recently, Pastorello et al. (2019a) alternatively proposed SN 1997bs to be a stellar merger. Another impostor, SN 2000ch, is thought to have a progenitor similar to Eta Carinae and at its peak of $M_V \simeq -12.7$ it showed an FWHM of the Balmer lines of up to $\sim$1550 km s^{-1} (Filippenko 2000; Wagner et al. 2004). It is important to note that SN impostors can also arise from lower-mass stars, such as SN 2008S and similar events (Kochanek et al. 2012), whose nature and that of other transients like it is still under debate (they might have been real CCSNe; see, e.g., Kochanek 2011; Adams et al. 2016; Cai et al. 2018, 2021). These transients have dust-enshrouded progenitors and ZAMS masses of $\sim$6–10 $M_\odot$ (Prieto et al. 2008; Thompson et al. 2009).

A remarkable example of the confusion between real CCSNe and impostors is SN 2009ip. When discovered in 2009 (Maza et al. 2009) it was classified as a Type IIn SN, reaching an absolute magnitude of $M_R \sim -14.5$. One year later, another bright eruption with similar luminosity was detected (Pastorello et al. 2013), indicating that the progenitor was still alive and did not experience a core-collapse event in 2009. These eruptions had, in fact, many similarities with LBVs, showing velocities of a few hundred km s^{-1}, although faster material with thousands of km s^{-1} was also observed. Analysis of prediscovery images suggested that the progenitor star of SN 2009ip was a very massive star with 50–80 $M_\odot$, showing LBV-like variability in the years before the 2009 eruption (Smith et al. 2010; Foley et al. 2011).

In 2012, SN 2009ip had two bright explosive events, reaching $M_V \sim -14.5$ in August (usually labeled Event A), and $M_R \sim -18$ in October (called Event B). Several authors have discussed the nature of the luminous event (Fraser et al. 2013; Pastorello et al. 2013; Mauerhan et al. 2013). Mauerhan et al. (2013) claimed that the high velocities detected in the outburst are evidence for a true CCSN during an LBV-like activity. Pastorello et al. (2013), however, argued that such high velocities were also observed during the 2011 event, which was clearly not a true SN. This scenario was also supported by Fraser et al. (2013), who showed that there was no signal of nebular emission from nucleosynthesis products after the 2012B eruption, although nebular emission could be hidden by the continuing interaction with CSM.

In the subsequent years, new analyses and a number of new observations have contributed to the discussion of whether the 2012 eruptions of SN 2009ip were a terminal event or not (Fraser et al. 2013, 2015; Prieto et al. 2013; Graham et al. 2014; Levesque et al. 2014; Margutti et al. 2014; Mauerhan et al. 2014; Smith et al. 2014; Moriya 2015; Thoene et al. 2015; Smith et al. 2016a; Graham et al. 2017). A number of newly detected transients also presented very similar behavior to SN 2009ip. SN 2010mc, classified as a Type IIn SN (Ofek et al. 2013), shows a nearly identical light curve to 2009ip, with precursor variability, a decline after peak consistent with ^{56}Co decay, and late-time flattening in the light curve due to CSM interaction. Smith et al. (2014) claimed that SN 2010mc was, in fact, a core-collapse event, arguing that the missing nebular phase is explained by CSM obscuration and that a nonterminal event with energies of $\sim 10^{50}$ erg is implausible. SN 2016bdu (Pastorello et al. 2017) also had spectroscopic features of Type IIn SNe, with several similarities to SN 2009ip, including the remarkably similar light curve for its two explosive events. Prediscovery images also showed progenitor variability similar to that of SN 2009ip. SN 2018cnf (Pastorello et al. 2019b) also had a sequence of two bright outbursts, after years of explosive variability with eruptions reaching $M_r \sim -14.7$. Pastorello et al. (2019b) proposed a massive hypergiant or an LBV star as a plausible progenitor for SN 2018cnf. More recently, the event AT 2016jbu/Gaia 16cfr showed a variable behavior followed by two bright outbursts (Kilpatrick et al. 2018; Brennan et al. 2021a, 2021b). The availability of prediscovery images from the Hubble Space Telescope (HST) allowed Brennan et al. (2021a, 2021b) to estimate that the progenitor star had a relatively low mass of $\sim$20 $M_\odot$. Other notable SN 2009ip–like transients might include SN 2015bh (Elias-Rosa et al. 2016; Thöne et al. 2017; Boian & Groh 2018), SN Hunt 151 (Elias-Rosa et al. 2018), LSQ 13zm (Tartaglia et al. 2016), and SN 2013gc (Reguitti et al. 2019).

The growing class of SN 2009ip–like transients show several observational similarities: (i) erratic prediscovery variability, sometimes including LBV-like outburts; (ii) two luminous eruptive events, with the second peak reaching ~ -18 mag; and (iii) the spectroscopic properties of Type IIn SNe, including multiple velocity components observed in the Balmer lines.

Here, we present observations of SN 2011fh, which share many similarities to SN 2009ip. Discovered by amateur astronomer Berto Monard on 2011 August 24 from South Africa, SN 2011fh was classified as a Type IIn SN at peak by Prieto & Seth (2011). The source is located in the outskirts of the nearby galaxy NGC 4806. We describe our 10 years of observations of SN 2011fh in Section 2. Section 3 describes the host galaxy (Section 3.1), the photometric (Section 3.2) and spectroscopic (Section 3.3) evolution, and the environment where SN 2011fh is located (Section 3.4). We discuss our analysis in Section 4, and present a final summary of our conclusions in Section 5.

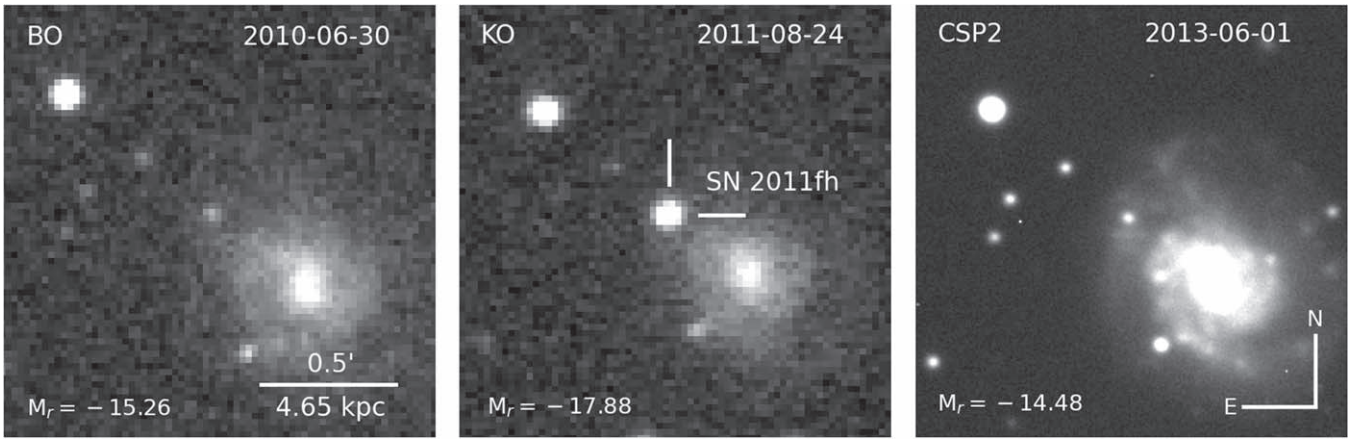

Figure 1. Unfiltered images of the galaxy NGC 4806 and SN 2011fh obtained by Berto Monard (left and middle panels) and an *r*-band CSP2 image at a later phase (right panel). SN 2011fh reached a peak absolute magnitude of $M_r = -17.88$ on 2011 August 24, as it is shown in the middle panel. The 0.′5 horizontal bar corresponds to 4.65 kpc at the distance of NGC 4806. The panels also show the UT date when the images were taken and the absolute *r*-band magnitude of SN 2011fh at that time.

2. Observations

SN 2011fh was discovered by amateur astronomer Berto Monard on 2011 August 24 UT[11] using unfiltered images from the Klein Karoo Observatory in South Africa (Monard et al. 2011), at ∼14.5 mag. The source was classified as a Type IIn SN at peak by Prieto & Seth (2011), using observations obtained with the du Pont 2.5 m telescope and the Wide Field reimaging CCD camera (WFCCD) at the Las Campanas Observatory (LCO) on 2011 August 28. A series of spectroscopic observations were obtained after peak brightness using the Apache Point Observatory (APO) 3.5 m telescope, the du Pont 2.5 m telescope, and the Magellan Baade and Magellan Clay 6.5 m telescopes. Photometric measurements were obtained by the Carnegie Supernova Project-II (CSP2, Hamuy et al. 2006; Phillips et al. 2019; Stritzinger et al. 2020) using the Swope 1 m and du Pont 2.5 m telescopes, and archival data were retrieved from the Catalina Real-Time Transient Survey (CRTS, Drake et al. 2009) and amateur astronomers. We also analyze archival images obtained by the Spitzer Space Telescope (SST) and the Hubble Space Telescope (HST), as well as spectroscopic observations made with the Multi-Unit Spectroscopic Explorer (MUSE) instrument on the Very Large Telescope (VLT).

2.1. Optical and NIR Photometry

Archival unfiltered images obtained by amateur astronomers and CRTS span from 2007 to 2013 (Figure 1). Berto Monard obtained 27 unfiltered images between 2009 January 06 and 2013 January 22, using Meade 12 and 14 inch f/8 telescopes, and an SBIG ST-8 CCD with a pixel scale of 1.″6 pixel^{-1}. Five images were obtained by Stu Parker using a Celestron 14 inch f6.3 telescope with a pixel scale of 1.″1 pixel^{-1} and a Celestron 11 inch f6.3 telescope with a pixel scale of 1.″6 pixel^{-1}, both using an SBIG ST-10 3 CCD camera, between 2011 June 16 and August 09. Three images were also obtained by Greg Bock using a Meade 14 inch telescope, and an SBIG ST-10 Dual CCD Camera, with a pixel scale of 1.″1 pixel^{-1}, between 2011 June 21 and 2012 February 17. CRTS unfiltered images were all obtained by the Siding Springs Survey 0.5 m telescope with a pixel scale of 1.″8 pixel^{-1}.

[11] UT dates are used throughout this paper.

The unfiltered images were reduced using standard procedures, including bias and dark subtraction, and flat-fielding. The photometric measurements were made using point-spread function (PSF) fitting through DOPHOT (Schechter et al. 1993; Alonso-García et al. 2012). The measured fluxes were calibrated to CSP2 *r*-band magnitudes using stars in the field. The SDSS *r*-band was chosen because the emission is strongly dominated by Hα, as it is usual in transients arising from the interaction with hydrogen-rich CSM and also because this band is roughly at the midpoint of the wavelengths spanned by the unfiltered response function. The photometric measurements are presented in Table 8, and the *r*-band light curve of SN 2011fh is shown in Figure 2.

After peak, *BVri* images of SN 2011fh were obtained by the Carnegie Supernova Project-II (CSP2), with observations spanning from 2013 February 20 to 2016 January 14 using the direct imaging cameras of the du Pont 2.5 m telescope and the Henrietta Swope 1.0 m telescope (Figure 1) at LCO. Near-infrared (NIR) *YJH* images (Krisciunas et al. 2017) were taken between 2013 February 23 and 2017 May 16 with RetroCam on the du Pont telescope.

The CSP2 images were reduced using standard techniques in IRAF (Freedman & Carnegie Supernova Project 2005; Hamuy et al. 2006; Stritzinger et al. 2020). PSF photometry of SN 2011fh was extracted using DOPHOT, and the calibration used CSP2 photometry of standard stars in the field. The optical *BVri* photometry is reported in Table 9 and the NIR *YJH* photometry in Table 10. The CSP2 light curves of SN 2011fh are shown in Figure 2.

2.2. Spectroscopy

SN 2011fh was classified as a Type IIn SN ∼3 days after peak brightness using a spectrum obtained by the du Pont 2.5 m Telescope with the WFCCD camera. The spectrum was obtained using a 1.″7 slit with an FWHM resolution of ∼8 Å. Three other spectra obtained with the same instrument and similar configurations were taken on 2012 June 15, 2013 October 7, and on 2013 January 12. Four optical spectra were also obtained with the APO 3.5 m Telescope on 2012 January 01, 2012 February 29, 2012 April 29, and on 2013 March 18, using the Dual Imaging Spectrograph (DIS), with a 1.″5 slit and an FWHM resolution of ∼7 Å. A high-resolution spectrum

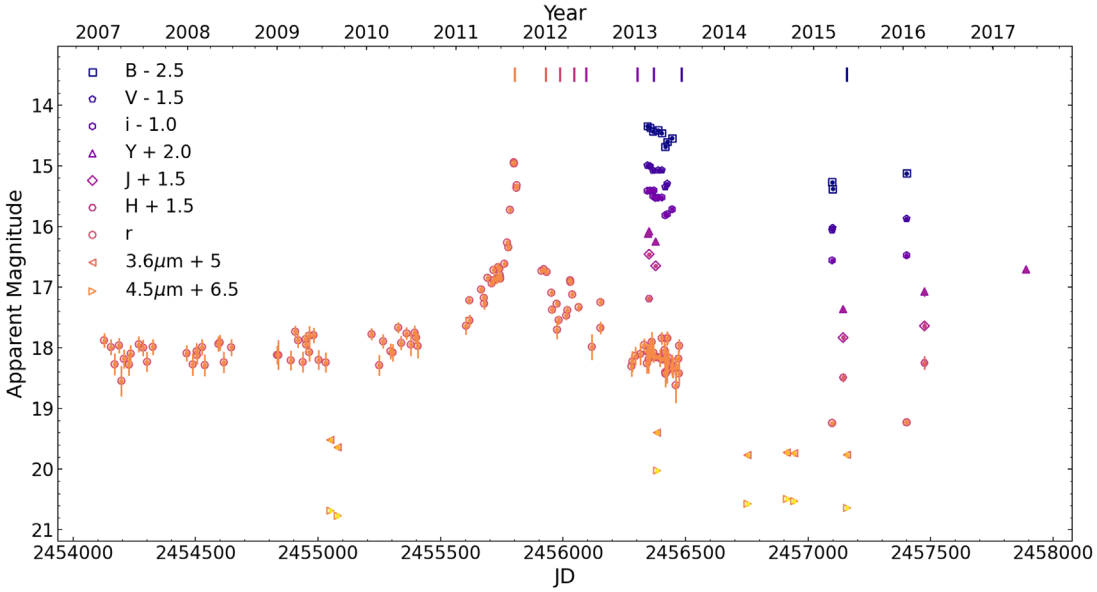

Figure 2. The complete photometry of SN 2011fh, including data from amateur astronomers, CRTS, CSP2, and the Spitzer Space Telescope. Unfiltered images from amateur astronomers and the CRTS were calibrated to the SDSS *r*-band magnitudes and span from 2007 January 25 to 2013 June 29. SN 2011fh was observed by the CSP2 from 2013 February 20 to 2017 May 16 using the *BVriYJH* filters. The Spitzer observations include early detections on 2009 August 6 and September 5, and five additional observations from 2013 March 31 to 2015 May 16. Spectra were obtained at the epochs marked as vertical lines at the top of the figure.

Table 1
Spectroscopic Observations of SN 2011fh

Phase (days) (1)	UT Date (2)	HJD (3)	Telescope/Instrument (4)	Slit Width (arcsec) (5)	Resolution (Angstrom) (6)	Wavelength Range (Angstrom) (7)
+3	2011-08-30	2,455,803.479	du Pont 2.5 m/WFCCD	1.7	8	3700–9120
+4	2011-08-31	2,455,805.479	Magellan Clay/MIKE	1.0	0.2	3500–9000
+129	2012-01-02	2,455,928.983	APO 3.5 m/DIS	1.5	7	3470–9520
+187	2012-02-29	2,455,986.895	APO 3.5 m/DIS	1.5	7	3570–9520
+246	2012-04-29	2,456,046.740	APO 3.5 m/DIS	1.5	7	3470–9520
+293	2012-06-15	2,456,093.612	du Pont 2.5 m/WFCCD	1.7	8	3470–9520
+505	2013-01-12	2,456,304.846	du Pont 2.5 m/WFCCD	1.7	8	3670–9225
+570	2013-03-18	2,456,369.840	APO 3.5 m/DIS	1.5	7	3480–9520
+600	2013-04-18	2,456,400.507	Magellan Baade/FIRE	0.6	24/36/73	8130–24740
+684	2013-07-10	2,456,484.465	du Pont 2.5 m/WFCCD	1.7	8	3670–9120
+1359	2015-05-17	2,457,159.037	VLT/MUSE	0.8	2.3	4710–9270

Note. Because the VLT/MUSE spectrum comes from integral field data, $0\farcs8$ is the radius of a circular aperture around the source in the datacube, not the slit width.

($\Delta\lambda = 0.2$ Å) was obtained with the Magellan Clay 6.5 m Telescope using the Magellan Inamori Kyocera Echelle (MIKE; Bernstein et al. 2003) spectrograph with a $1''$ slit on 2011 August 31. An additional near-infrared (NIR) spectrum was obtained with the Folded port InfraRed Echellette (FIRE; Simcoe et al. 2013) spectrograph on the Magellan Baade 6.5 m Telescope, using a $0\farcs6$ slit, and the high-throughput prism mode, which gives continuous coverage from 0.8–2.5 μm and resolutions of $R \sim 500$, 450, and 300 in the *JHK* bands, respectively.

The low-resolution optical spectra were reduced using standard techniques in the IRAF `twodspec` and `onedspec` packages. We also applied a constant flux calibration correction to the spectra to match the synthetic *r*-band photometry to the light curve. The MIKE high-resolution spectrum was reduced using the CarPy reduction pipeline. The NIR FIRE observations were obtained using an ABBA nodding sequence and a bright A0V star close to the target in the sky was used as a flux and telluric standard. The spectrum was reduced using the IDL pipeline `FIREHOSE` (Simcoe et al. 2013).

The spectra are summarized in Table 1, including the dates, instruments, and configurations used for the observations. The spectral evolution of SN 2011fh is shown in Figure 3, and the NIR FIRE spectrum is shown in Figure 4.

2.3. Spitzer Imaging

After SN 2011fh was discovered, Spitzer/IRAC (Fazio et al. 2004) 3.6 and 4.5 μm archival images from 2009 August and September (Program 6007; PI: K. Sheth) revealed a mid-infrared source at the position of the SN (Monard et al. 2011). Five more images using the 3.6 and 4.5 μm channels were taken from 2013 to 2015 (Programs 90137, 10139, 11053, PI: O. Fox). We downloaded the calibrated PBCD images from the Spitzer Heritage Archive[12] and performed PSF photometry

[12] https://sha.ipac.caltech.edu/applications/Spitzer/SHA/

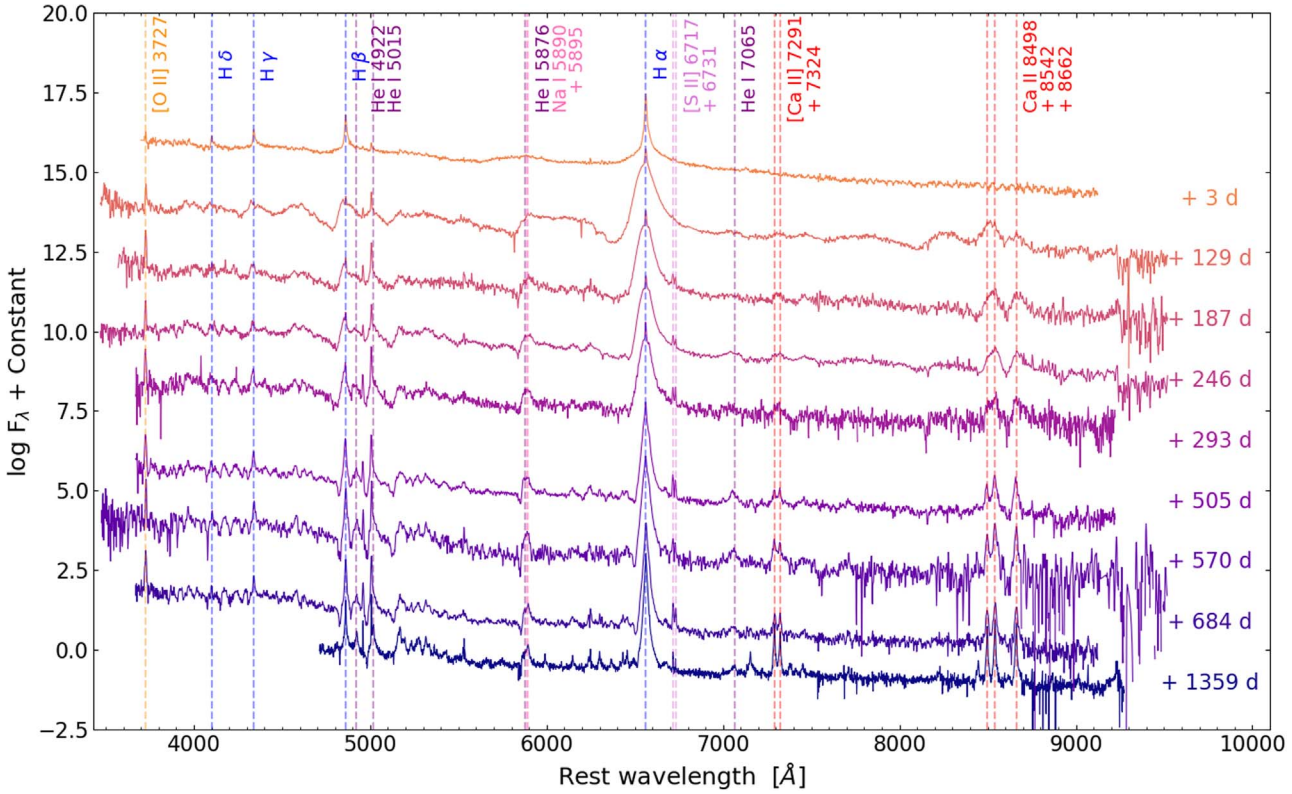

Figure 3. The spectral evolution of SN 2011fh from 3 (top) to 1359 (bottom) days after peak brightness. The wavelength is in the rest frame, and we show $\log_{10}F_\lambda$ plus an offset. The phase is relative to maximum brightness in the *r* band. Prominent lines of H, He I, Ca II, Na I, [S II], and [O II] are highlighted with dashed lines. The spectra at phases +3 days, +293 days, +505 days, and +684 days were obtained by the du Pont 2.5 m + WFCCD, and the spectra at phases +129 days, +187 days, +246 days, and +570 days by the APO 3.5 m + DIS instrument (Table 1). The last spectrum, at phase +1359 days, was extracted from VLT + MUSE observations. All the spectra presented in this figure are available in WISeREP (https://www.wiserep.org/; Yaron & Gal-Yam 2012).

using DOPHOT. The result of our photometry is reported in Table 11. The 3.6 and 4.6 μm evolution of SN 2011fh is also shown in Figure 2. The Spitzer/IRAC photometry of SN 2011fh 586 days after peak was also presented by Szalai et al. (2019) and is fairly consistent with our results.

2.4. HST Imaging

SN 2011fh was observed by HST on 2016 October 20 (proposal ID 14149; PI: A.V. Filippenko) using the Wide Field Camera 3 (WFC3) Ultraviolet-Visible (UVIS) channel, and the F336W and F814W filters with exposure times of 710 s and 780 s, respectively. The data were retrieved from the Mikulski Archive for Space Telescopes (MAST). PSF photometry on the calibrated `flt` images was performed with `DOLPHOT` (Dolphin 2016), using the drizzled F814W image as a reference for point-source detection and astrometry. We selected point sources using the `DOLPHOT` parameter criteria of Williams et al. (2014): sharpness$^2 \leqslant 0.15$, crowding $\leqslant 1.0$, and signal to noise $\geqslant 5$. The F814W image is shown in Figure 5 with an inset zooming on the region around SN 2011fh. We measured the WFC3 Vega magnitudes of m(F336W) $= 18.956 \pm 0.006$ mag and m(F814W) $= 19.374 \pm 0.004$ mag for the SN.

2.5. MUSE Spectroscopy

Integral field spectroscopy of the galaxy NGC 4806 was obtained with MUSE (Bacon et al. 2014) on the VLT on 2015 May 17, at a phase of +1359 days (program ID:095.D-0172(A); Kuncarayakti et al. 2018). We retrieved the reduced wavelength- and flux-calibrated datacube from the ESO archive.[13] The cube has $0\farcs2 \times 0\farcs2$ spaxels, a seeing of $0\farcs8$, and a spectral range of 4750–9350 Å. We used a $0\farcs8$ radius aperture to extract the spectrum of SN 2011fh from the MUSE datacube. The spectrum is shown in Figure 3 and in Figure 6, where we highlight the emission lines observed at very late times.

3. Results

3.1. Host Galaxy

SN 2011fh is located at $\alpha = 12^{\rm h}56^{\rm m}14\overset{\rm s}{.}009$ and $\delta = -29°29'54\farcs82''$ (J2000.0), in one of the spiral arms of the nearby galaxy NGC 4806. The redshift for NGC 4806, obtained from the NASA-IPAC Extragalactic Database (NED),[14] is $z = 0.00803$ (Paturel et al. 2003). Using the heliocentric velocity for the galaxy of $v = 2408 \pm 4$ km s^{-1} (Paturel et al. 2003), and the Cosmicflows-3 distance-velocity calculator,[15] which has a flow model consistent with $H_0 = 75$ km s^{-1} Mpc^{-1} (Kourkchi et al. 2020), we get a distance of $D = 30.66$ Mpc. Because the model has a zero-point error of 3% (Kourkchi et al. 2020), we obtained an uncertainty in the distance of 0.92 Mpc. The distance modulus is therefore $\mu = 32.43 \pm 0.06$ mag.

We estimate the redshift at the position of SN 2011fh using the MUSE spectrum of the H II region around the SN. We used Gaussian fitting to estimate the central position of the emission

[13] http://archive.eso.org
[14] https://ned.ipac.caltech.edu
[15] http://edd.ifa.hawaii.edu/NAMcalculator/

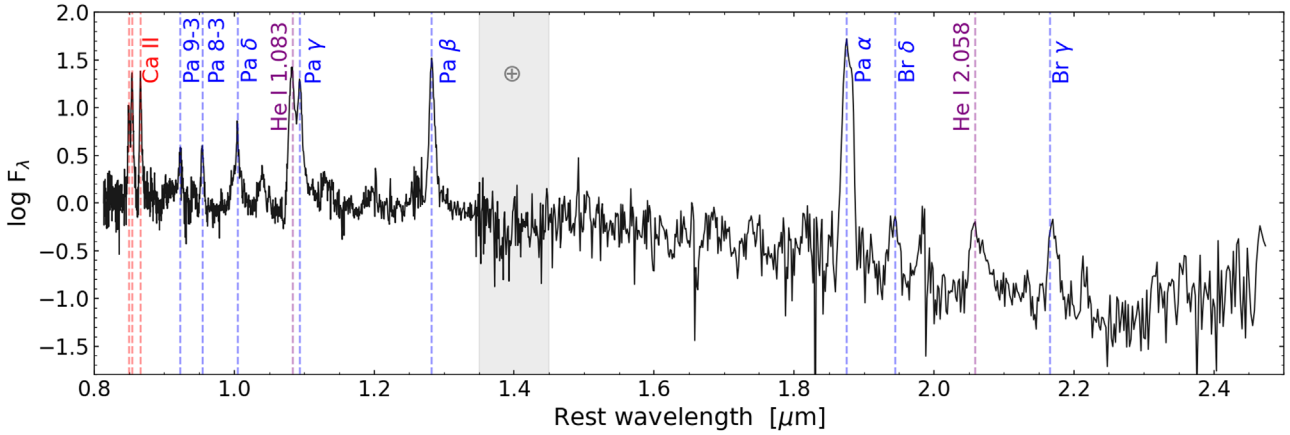

Figure 4. Rest-frame FIRE NIR spectrum of SN 2011fh obtained on 2013 April 18, 600 days after peak brightness. The spectrum is dominated by emission lines of hydrogen, with prominent Paschen series (Paα, Pa β, Pa γ, Pa δ, Pa 8−3, and Pa 9−3) and Brackett series (Br γ and Br δ) lines highlighted by the blue dashed lines. Lines of He I at 1.083 and 2.058 μm are marked by purple lines. The Ca II $\lambda\lambda$8498, 8542, 8662 triplet is marked by orange dashed lines. The gray band marks the region of the strong telluric absorption.

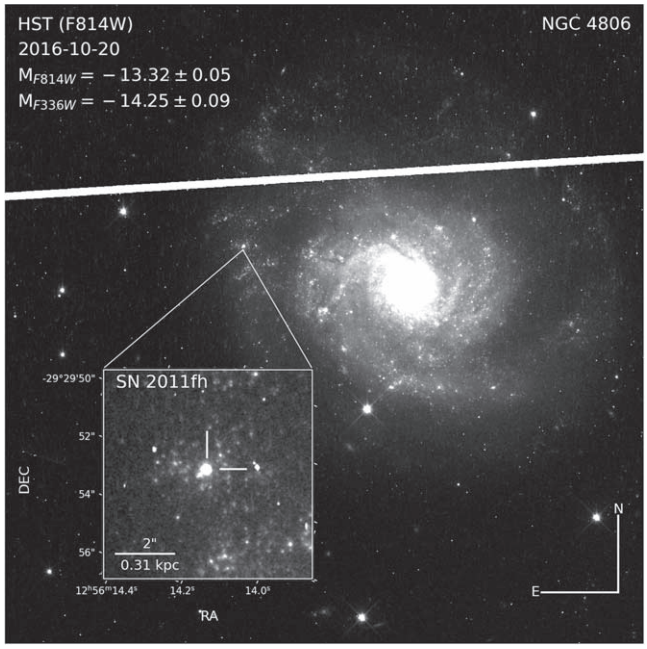

Figure 5. HST F814W image of NGC 4806 from 2016 October 20. The inset shows the region around SN 2011fh. The 2″ horizontal bar at the inset corresponds to 0.31 kpc at the position of SN 2011fh. SN 2011fh has absolute magnitudes of $M_{\rm F814W} = -13.32 \pm 0.05$ mag and $M_{\rm F336W} = -14.25 \pm 0.09$ mag.

lines of Hα, Hβ, [N II] $\lambda\lambda$6548, 6584 Å, [S II] $\lambda\lambda$6716, 6731 Å, and [O III] $\lambda\lambda$5007, 4959 Å and measured the local redshift of $z = 0.00812$. This is the value we consider throughout the paper.

The Milky Way (MW) extinction toward NGC 4806 is $A_V = 0.232$ mag (Schlafly & Finkbeiner 2011) and $E(B-V) = 0.0748$ mag, with $R_V = 3.1$. We estimate the host-galaxy extinction using the high-resolution MIKE spectrum. The interstellar Na I doublet (Na I D) absorption lines from the galaxy have equivalent widths (EWs) of 0.1231 Å for Na D1 and 0.1966 Å for Na D2. By scaling these values with the EWs of the MW Na I D absorption features (0.1118 Å and 0.1902 Å for Na D1 and D2, respectively), we obtained $A_V = 0.24$ mag or $E(B-V) = 0.078$ mag for the host galaxy. Thus, using the 2% photometric error in the measurements of Schlafly & Finkbeiner (2011) and assuming a 10% uncertainty in the host extinction, the total estimated V-band extinction for SN 2011fh is $A_V = 0.48 \pm 0.03$ mag.

We also estimated the extinction of the cluster of stars near SN 2011fh. We use a spectrum extracted with a 2″–3″ annulus aperture from the MUSE datacube and measured a Balmer decrement of Hα/H $\beta = 3.34$. Using Levesque et al. (2010), this value implies a total $E(B-V) = 0.16$ mag or $A_V = 0.49$ mag. Because this result is consistent with the total estimated extinction for SN 2011fh, we decided to use the same value of $A_V = 0.48$ mag for the stars surrounding the SN.

3.2. Photometric Evolution

Figure 2 shows the complete photometric evolution of SN 2011fh from 2007 to 2017. The SN reached peak r-band brightness on 2011 August 24 (JD = 2,455,799), at $r = 14.94 \pm 0.02$ mag, or $M_r = -17.88 \pm 0.04$ mag.[16] Before peak, a five-month-long (173 days) brightening event is observed, where the progenitor goes from $r = 17.63 \pm 0.15$ on 2011 February 11, to $r = 16.26 \pm 0.04$ on 2011 July 28. After this slow brightening, the source shows a rapid increase to $r \sim 14.94$ mag over $\sim$40 days, culminating in the August peak.

A precursor event followed by a rapid rise to peak brightness is commonly seen in 2009ip–like transients. For this class of transients, the initial rise is commonly called "Event A," and the main peak is called "Event B." In Figure 7, we show the r-band light curve near peak brightness of SN 2011fh, SN 2009ip (Fraser et al. 2013; Mauerhan et al. 2013), SN 2016bdu (Pastorello et al. 2017), and SN 2018cnf (Pastorello et al. 2019b). The Vega R-band magnitudes of SN 2009ip were scaled to AB magnitudes by adding 0.21 mag (Blanton & Roweis 2007). The four transients show a remarkably similar absolute magnitude at peak, with $M_r = -18.29 \pm 0.10$ for SN 2009ip, $M_r = -18.00 \pm 0.16$ for SN 2016bdu, and $M_r = -18.25 \pm 0.05$ for SN 2018cnf. SN 2009ip and SN 2016bdu have a very similar Event A, peaking at $M_r \sim -15.5$ and lasting

[16] For the uncertainty in the absolute magnitudes, we took into account the estimated error in the apparent magnitude, the 3% uncertainty in the distance given by Kourkchi et al. (2020), and the 2% error in color estimated by Schlafly & Finkbeiner (2011).

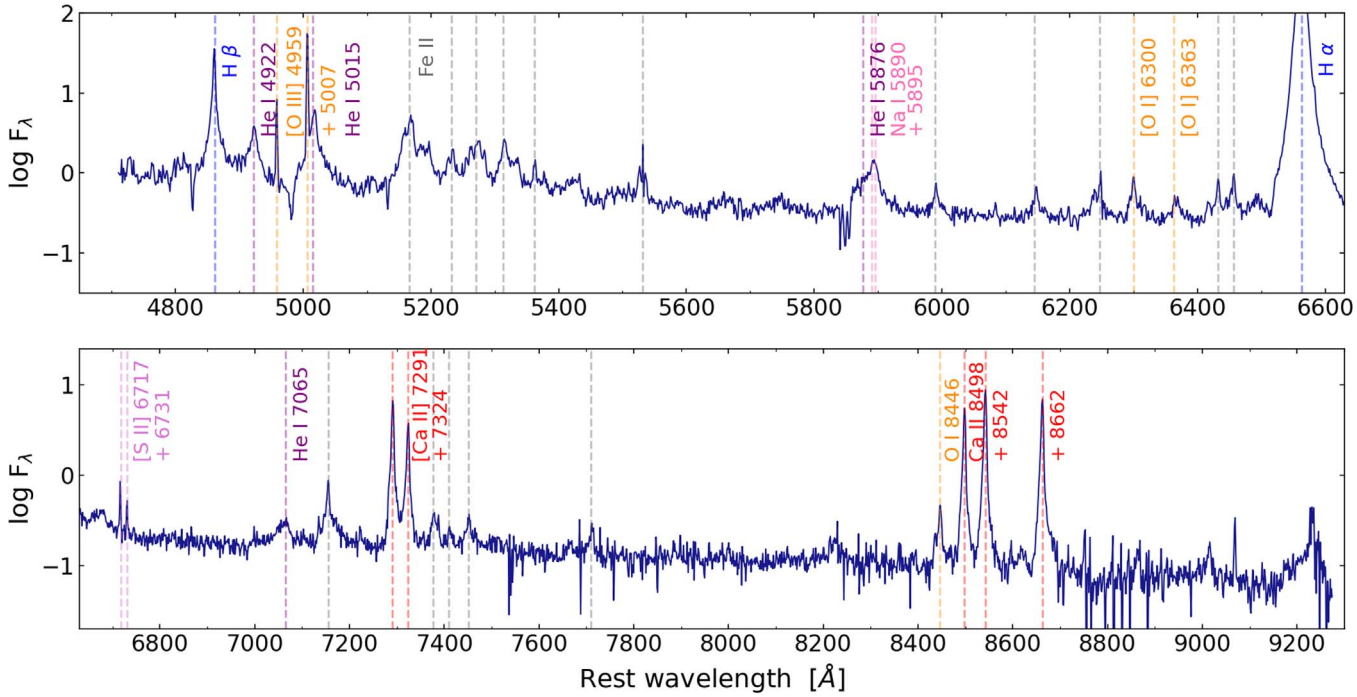

Figure 6. The rest-frame VLT/MUSE spectrum of SN 2011fh obtained on 2015 May 17, 1359 days after peak brightness. Lines of H, He I, Ca II, Na I, [O I], [O III], [S II], and Fe II are highlighted. Forbidden lines of [O III] and [S II] are most likely due to host-galaxy contamination.

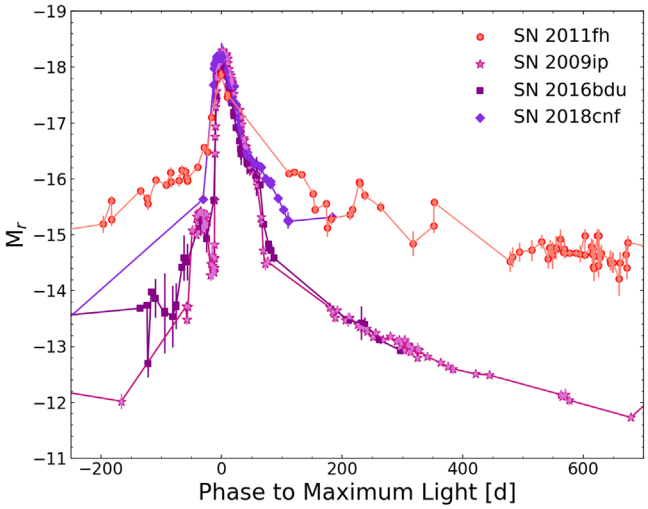

Figure 7. Comparison of the *r*-band light curve near peak brightness of SN 2011fh to SN 2009ip (Fraser et al. 2013; Mauerhan et al. 2013), SN 2016bdu (Pastorello et al. 2017), and SN 2018cnf (Pastorello et al. 2019b). The phase is in days relative to peak brightness.

for ∼40 days. Although different in brightness and duration, the slow increase in luminosity seen for SN 2011fh before peak might share a similar origin to the other transients. After the precursor Event A, all four transients show a rapid brightening to peak, over ∼15 days for SN 2009ip, ∼25 days for SN 2016bdu, and ∼30 days for SN 2018cnf. It is worth noting that the magnitude difference between the end of Event A and the peak brightness is considerably larger for the other transients.

Before the explosive events of 2011, the source of SN 2011fh is seen to be bright, with an apparently constant luminosity over the preceding three years (see Figure 2). The images are relatively shallow, so it is hard to tell whether the variability is real or not. The absolute magnitudes of $M_r \sim -14.5$ to $M_r \sim -15.5$ are very high in the years preceding the major brightening event. For comparison, the progenitors of SN 2009ip and SN 2016bdu had *r*-band absolute magnitudes of −13 to −14 mag.

The stellar cluster around SN 2011fh might be a source of photometric contamination in the pre-outburst images, which were all obtained using cameras with large pixel scales. We estimate the photometric contamination in Appendix A. Our analysis shows that the contribution of the stellar cluster is not a serious problem, although it increases for the bluer bands.

Spitzer imaging from 2009 also reveals a bright source at the position of SN 2011fh. Photometry of the 3.6 and 4.5 μm channels show a source with apparent magnitudes of 15.9 and 15.5, respectively. These imply luminosities of 3.5×10^6 and $2.5 \times 10^6\, L_\odot$, respectively. In the discovery report, Monard et al. (2011) noted that the mid-IR luminosity may have a contribution from the H II region around the source, due to the 260 pc spatial resolution of the IRAC instrument.

During the first days after peak, the brightness of SN 2011fh drops significantly. Unfortunately, between 7 and 110 days after peak in *r*-band, there were no photometric observations of the source. After 110 days, it is significantly fainter and slowly fading. The decay, however, is not monotonic, with two pronounced peaks at 228 (2012 April 11, or JD = 2,456,029) and 350 days (2012 August 12, or JD = 2,456,151) after peak (Figure 7). Bumps and fluctuations after peak brightness are common in the light curve of SN 2009ip–like objects, but the amplitudes seen for the other three sources shown in Figure 7 are significantly smaller. This behavior is usually interpreted as the collision of the ejecta with circumstellar material showing a complex density profile. The overall evolution of SN 2011fh in the months following peak brightness is, however, very similar to SN 2009ip, with a slow fading probably caused by the ongoing interaction with a dense CSM.

The CSP2 optical *BVri*- and NIR *YJH*-band images of SN 2011fh, as well as new IR Spitzer observations, were obtained only starting ∼550 days after peak (2013 February 20). The behavior in the other filters is very similar to that in the *r* band. Initially, all bands show a slow drop in brightness, with an apparent flattening by the beginning of 2015, 1300 days after peaking in the *r* band. At this epoch, the source is still quite luminous, with $M_r \sim -13.5$ mag. Surprisingly, an apparent rise in luminosity is detected by the beginning of 2016 in the optical *BVi* and NIR *YJH* bands, although not in the *r* band. The apparent brightening in the NIR bands is clear in the last point of the light curve where the *Y*-band brightened by $\Delta Y \approx 0.36$ mag over 418 days.

HST observations from October 2016 show a very bright source at the position of SN 2011fh (Figure 5), with absolute magnitudes of $M_{\rm F814W} = -13.32 \pm 0.05$ mag and $M_{\rm F336W} = -14.25 \pm 0.09$ mag. This is much more luminous than even the most-luminous quiescent stars known (e.g., R136a1 and BAT 99-98 in the Tarantula Nebula of the Large Magellanic Cloud, with absolute bolometric magnitudes of −12.2 and −12.0, respectively; Bestenlehner et al. 2020; Hainich et al. 2014). Another parallel can be made with Eta Carinae, which reached an absolute magnitude of $M_V \sim -14$ mag during its 19th Century Great Eruption (Smith et al. 2018a). This might be simply due to late-time emission due to the ongoing interaction of the ejecta with the CSM, as it is commonly seen for interacting transients (e.g., Graham et al. 2017), or alternatively indicate that we are seeing the star in an LBV-like eruptive state.

3.2.1. Colors

Figure 8 shows the CSP2 $B-V$, $r-i$, $J-H$, and the [3.6] − [4.5] color evolution of SN 2011fh. For the optical and near-IR bands, unfortunately, we only have colors at very late times, starting at 550 days after the maximum brightness. We are able to estimate the mid-IR colors of the progenitor 750 days before peak brightness.

As commonly seen for Type IIn SNe, the $B-V$ and $r-i$ evolution of SN 2011fh is very slow (Taddia et al. 2013). The $B-V$ color becomes slightly bluer, consistent with the temperature increase measured in the spectra and the overall spectral energy distribution (SED; see Section 3.2.2 and Section 3.3). The $J-H$ color becomes slightly redder, increasing from 0.22 mag, at phase +550 days, to 0.34 mag, at phase +1676 days, although this last value has large uncertainties.

Type IIn SNe are usually bright in the mid-IR bands and have very heterogeneous properties (Szalai et al. 2021). A significant color evolution is seen for SN 2011fh in the mid-IR if we compare the values before and after the luminous outburst of 2011. The source has [3.6] − [4.5] = 0.37 mag at phase −715 days, and [3.6] − [4.5] = 0.87 mag, 580 days after peak. After peak, the mid-IR color becomes a little redder, decreasing slowly with time.

We also show the $B-V$ and $R-I$ evolution of SN 2009ip in Figure 8 from Fraser et al. (2015). We show the $R-I$ colors because $r-i$ is not available for these epochs. The Vega *R*- and *I*-band values were scaled to AB magnitudes by adding, respectively, 0.21 mag and 0.45 mag (Blanton & Roweis 2007). In $B-V$, SN 2011fh is significantly bluer than SN 2009ip, although both events become redder with time. This might be due to the fact that SN 2011fh is located in a blue star-forming region, with the contamination from the cluster increasing as the SN fades (see Appendix A). The other possible explanation is that SN 2011fh is intrinsically hotter than SN 2009ip. The $R-I$ colors of SN 2009ip are redder than the $r-i$ values for SN 2011fh. This might imply that SN 2009ip has stronger Hα emission lines in relation to the spectral continua throughout its evolution. SN 2009ip has a very similar mid-IR color evolution to SN 2011fh. Although the mid-IR estimates are uncertain at late times, SN 2009ip becomes a little redder after peak, and then bluer around a phase of ∼1000 days (Szalai et al. 2019, 2021).

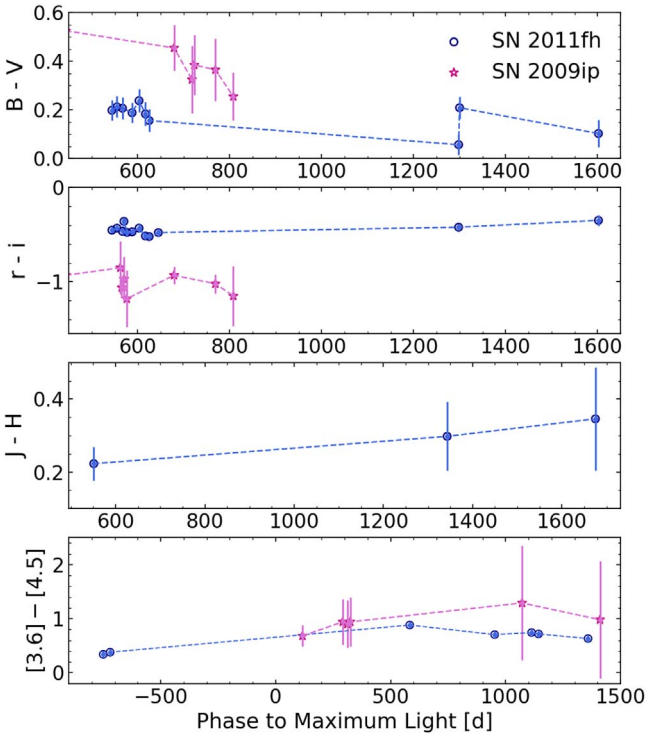

Figure 8. $B-V$, $r-i$, $J-H$, and [3.6] − [4.5] color evolution of SN 2011fh. Phase is in days relative to *r*-band peak. For comparison, we also show the $B-V$, $R-I$, and [3.6] − [4.5] color evolution of SN 2009ip (Fraser et al. 2015; Szalai et al. 2019). We show the $R-I$ color because $r-i$ data are not available.

3.2.2. Spectral Energy Distribution

We use the optical, near-infrared (NIR), and infrared (IR) photometry to constrain the SED of SN 2011fh after peak. We used SUPERBOL (Version 1.7; Nicholl 2018) to estimate the blackbody temperature, luminosity, and photosphere radius between phases +544 and +1602 days. Because SN 2011fh has very strong Hα emission (see Section 3.3), we carried out this first analysis using only the optical *BVi* bands. The results of the single-blackbody fits to these three filters are shown in Figure 9 and reported in Table 2.

SN 2011fh has an unusual temperature evolution for either an SN or a SN impostor. Transients driven by CSM interaction usually show a smooth decrease in temperature after peak (Margutti et al. 2014; Kilpatrick et al. 2018), opposite to the behavior of SN 2011fh. The blackbody temperature at phase +544 days is $T_{\rm BB} \approx 8920$ K, and it rises to $T_{\rm BB} \approx 9950$ K at phase +630 days. A higher blackbody temperature of ∼11000 K is measured at 1300 days, but the late-time measurements are uncertain and the fluxes may be dominated

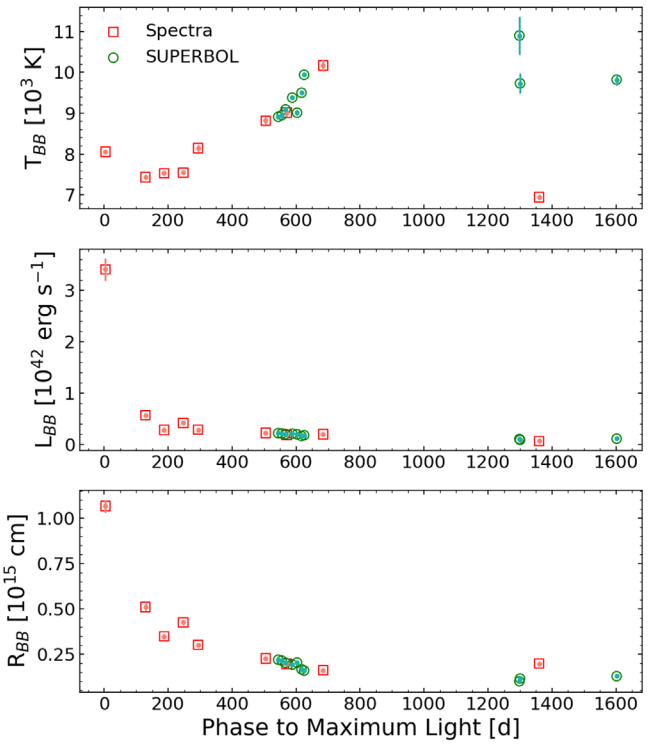

Figure 9. Temperature (T_{BB}), bolometric luminosity (L_{bol}), and radius (R_{BB}) evolution of SN 2011fh, estimated from blackbody fits to the spectral continua using Astropy models (red squares) and to the SEDs using SUPERBOL (green circles). The phase is relative to the maximum r-band luminosity in days.

Table 2
SUPERBOL Fits to the *BVi* Bands

Phase	T_{BB}		10^{41} L_{BB}		10^{14} R_{BB}	
(days)	(K)	(error)	(erg s^{-1})	(error)	(cm)	(error)
(1)	(2)	(3)	(4)	(5)	(6)	(7)
+544	8910	55	2.17	0.11	2.20	0.15
+555	8950	105	2.12	0.15	2.15	0.15
+566	9090	74	2.00	0.10	2.03	0.14
+587	9380	58	2.07	0.27	1.93	0.16
+602	9010	76	1.95	0.24	2.04	0.14
+616	9500	38	1.62	0.17	1.67	0.16
+625	9940	27	1.78	0.08	1.60	0.11
+1298	10900	465	1.03	0.11	1.01	0.08
+1300	9730	246	0.86	0.05	1.16	0.08
+1602	9820	147	1.10	0.05	1.29	0.07

by line emission at these epochs (see Figure 3 and Section 3.3). The radius evolution of SN 2011fh also differs from the usual increase and then smooth decrease after peak. The evolution of the photospheric radius of SN 2009ip was also unusual and was interpreted by Margutti et al. (2014) as being due to a more complex CSM structure.

We also model the SED using DUSTY (Ivezic & Elitzur 1997), a code for solving radiative transfer through a spherically symmetric dusty medium. We assume a central stellar source using atmospheric models from Castelli & Kurucz (2003), a dust shell with a thickness $R_{out}/R_{in} = 2$, and silicate dust from Draine & Lee (1984) with a standard Mathis, Rumpl, and Nordsieck (MRN) dust size distribution (Mathis et al. 1977). We find best-fitting models using a MCMC wrapper around DUSTY as in Adams & Kochanek (2015). In Table 3 we show the resulting photospheric (T_{phot}) and dust (T_{dust}) temperatures, together with the estimated photospheric radius (R_{phot}) and inner radius of the dust shell ($R_{in,dust}$), the total luminosity (L), and the dust optical depth in V band (τ_V). Figure 10 shows the optical, NIR and IR SED, and the DUSTY fits at phase +570 days. At this period, the SED was fit with $\tau_V = 0.68$, $T_{phot} \approx 7865$ K, $T_{dust} \approx 950$ K, and $L \approx 10^{7.74}\,L_{\odot}$. The dust emission increases in temperature with time, reaching ~1116 K at phase +1143 days.

3.3. Spectroscopic Evolution

In Figure 3, we show the complete spectral evolution of SN 2011fh from 3 to 1359 days after peak brightness. We use vertical lines to highlight prominent emission features of H, He I, Ca II, Na I, [S II], and [O II]. The spectra are dominated by Balmer lines in emission during the whole evolution, with features of He I and Ca II becoming more prominent with time. The forbidden lines of [S II] and [O II] seen throughout the evolution of SN 2011fh are most likely due to host-galaxy contamination. In Figure 11, we show the evolution of the emission profiles of Hβ, He I λ5876, the [Ca II] $\lambda\lambda$7291, 7324 doublet, and the Ca II $\lambda\lambda$8498, 8542, 8662 triplet.

Due to the different emission mechanisms, interacting transients can show very complex Balmer line profiles (see the review by Smith 2017). For the spectra of SN 2011fh, we used Astropy (Astropy Collaboration et al. 2013, 2018) to fit the Hα emission profiles with narrow Gaussian components and intermediate Lorentzian components, plus a constant continuum, as shown in Figure 12. The estimated FWHM velocity and the luminosity of the two components throughout the evolution of SN 2011fh are shown in Figure 13 and reported in Tables 4 and 5. Errors are estimated by the 1σ parameter uncertainty for the best-fitting Lorentzian and Gaussian models. A 3% uncertainty is also considered for the error in the luminosity of the components. Due to its proximity to the spectral resolution, the FWHM of the narrow components are corrected by the resolution value. At some epochs, the width of the narrow component falls below that value and is indicated as less than the spectral resolution in Table 4 and Figure 13. Prominent blue absorption features are also seen at certain epochs, especially at phases +129 and +187 days. The photospheric temperature, radius, and bolometric luminosity evolution of SN 2011fh, obtained from the spectral continuum fitting, also shown in Figure 9 and reported in Table 6, agree well with the SED models. Errors in temperature are given by the 1σ parameter uncertainty for the best-fitting model, while for the error in luminosity and radius, a 3% uncertainty in the distance is also considered.

The first spectrum in our sequence, obtained 3 days after peak, is dominated by Balmer lines in emission and resembles a typical Type IIn SN. It has a blue continuum with a blackbody temperature of $T_{BB} \sim 8000$ K. The Hα profile can be fit with an intermediate-width Lorentzian profile with an FWHM velocity of $v_{FWHM} \sim 2263$ km s^{-1}, and a narrow Gaussian component with $v_{FWHM} \sim 204$ km s^{-1}. The narrow Gaussian emission is generated by the ionized dense CSM, while the Lorentzian profile is indicative of broad electron scattering in the unshocked CSM (Chugai 2001).

The Hα profile becomes significantly broader in the second spectrum at +129 days. The Lorentzian profile now has $v_{FWHM} \sim 3376$ km s^{-1}, and the narrow Gaussian has

Table 3
DUSTY Fits of the SEDs

Phase (days) (1)	τ_V (2)	T_{phot} (K) (3)	T_{phot} (1σ error) (4)	T_{dust} (K) (5)	T_{dust} (1σ error) (6)	log L ($L_\odot$) (7)	log L (1σ error) (8)	log R_{phot} ($R_\odot$) (9)	log R_{phot} (1σ error) (10)	log $R_{in,dust}$ (cm) (11)	log $R_{in,dust}$ (1σ error) (12)
+570	0.68	7865	511	950	320	7.74	0.04	3.60	0.04	16.52	0.29
+1113	0.91	8321	537	903	233	7.48	0.06	3.42	0.03	16.50	0.26
+1143	0.61	8823	779	1116	240	7.48	0.05	3.37	0.05	16.38	0.18
+1300	0.78	8915	635	1006	182	7.40	0.05	3.32	0.04	16.44	0.17

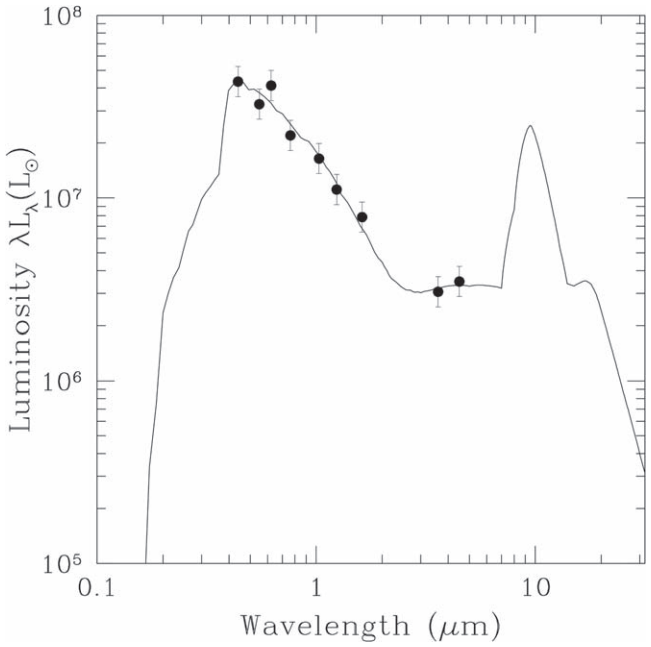

Figure 10. DUSTY fit to the SED at phase +570, using the optical and Spitzer data. The photospheric temperature is ~7865 K, and the dust temperature is ~950 K. The fit parameters are given in Table 3.

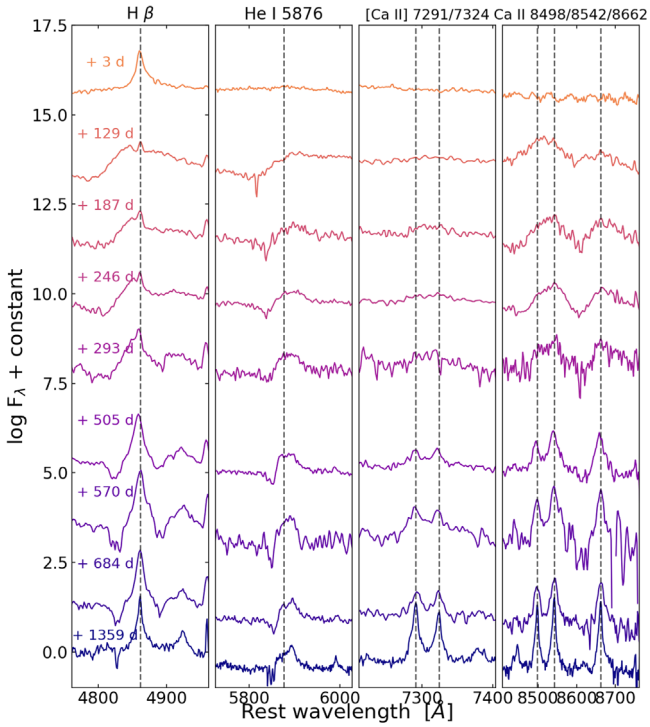

Figure 11. Evolution of Hβ, He I λ5876, the [Ca II] $\lambda\lambda$7291, 7324 doublet, and the Ca II $\lambda\lambda$8498, 8542, 8662 triplet. The vertical dashed lines mark the rest wavelengths.

$v_{FWHM} \sim 197$ km s^{-1}. The line is well described by a P Cygni profile with a strong blueshifted absorption feature. The blueshifted absorption wing extends to ~6430 km s^{-1}, and is probably formed by fast-moving material along the line of sight. At this epoch, the He I features and the Ca II triplet start to develop, with Hβ blended into the He I λ4922 emission line. The continuum becomes relatively redder, with a blackbody temperature of $T_{BB} \sim 7400$ K.

The FWHM of the Hα Lorentzian begins to decrease at +187 days, with $v_{FWHM} \sim 3087$ km s^{-1}, and the narrow Gaussian component is below the spectral resolution of ~320 km s^{-1}. The blueshifted absorption feature is still present, with a velocity of ~6447 km s^{-1}. The blackbody temperature remains almost constant, with $T_{BB} \sim 7500$ K.

By 293 days, the P Cygni absorption feature is no longer easy to identify, although the Hα line cannot be entirely described by only emission features, as can be seen in Figure 12. We measure $v_{FWHM} \sim 2568$ km s^{-1} for the Lorentzian component. This epoch is marked by a sudden inversion in temperature to $T_{BB} \sim 8100$ K. At this epoch, the emission features of Ca II become more prominent, with the [Ca II] $\lambda\lambda$7291, 7324 doublet beginning to develop and the three components of the Ca II $\lambda\lambda$8498, 8542, 8662 triplet becoming easily distinguishable.

The emission features remain very similar during the three next epochs, with He I and Ca II now very prominent. At phase +505 days, the Ca II λ8662 line can be fit with a narrow Lorentzian profile with $v_{FWHM} \sim 583$ km s^{-1}. The Fe II emission-line forest is also detected and becomes stronger in the last spectrum of our sequence (see Figure 6). At +684 days, the Hα profile gets considerably narrower, with $v_{FWHM} \sim 925$ km s^{-1} for the Lorentzian component. At this time, the blackbody temperature reaches its maximum measured value of $T_{BB} \sim 10{,}200$ K.

The unusual temperature increase seen in SN 2011fh, in both SEDs and the spectral continua, might be generated by the shock interacting with the CSM, a scenario that might be supported by the bumps seen in the *r*-band light curve. Another possibility is that the CSM is becoming relatively thin, revealing a hot stellar photosphere.

The NIR spectrum taken on 2013 April 18, 600 days after peak (Figure 4) shows prominent emission lines of the Paschen and Brackett series, and features from He I and Ca II. This was also observed in early NIR spectroscopy of the Event B in SN 2009ip (Pastorello et al. 2013; Smith et al. 2013; Margutti et al. 2014). Although our spectrum was taken in a much later time

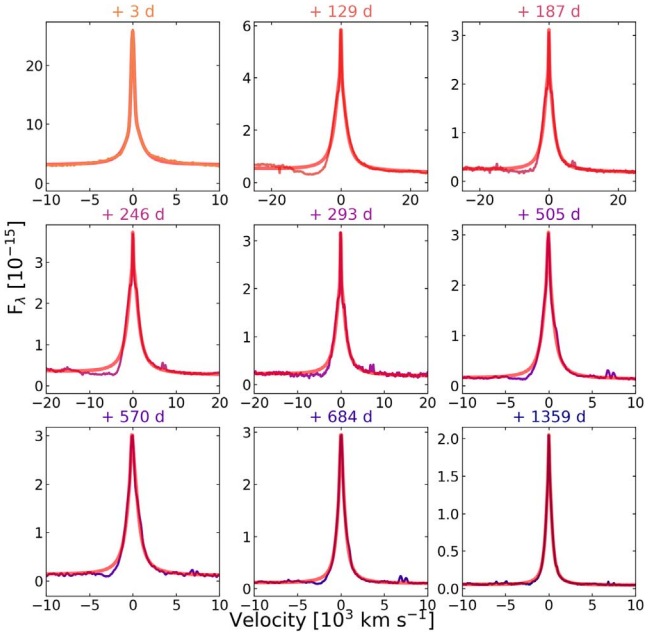

Figure 12. Evolution of the Hα emission line and a model built with a narrow-width Gaussian component and an intermediate-width Lorentzian component. Velocity corresponds to the rest-frame wavelength of Hα, and the spectral phases are given above each panel. Absorption features are seen in some epochs, especially at +129 and +187 days.

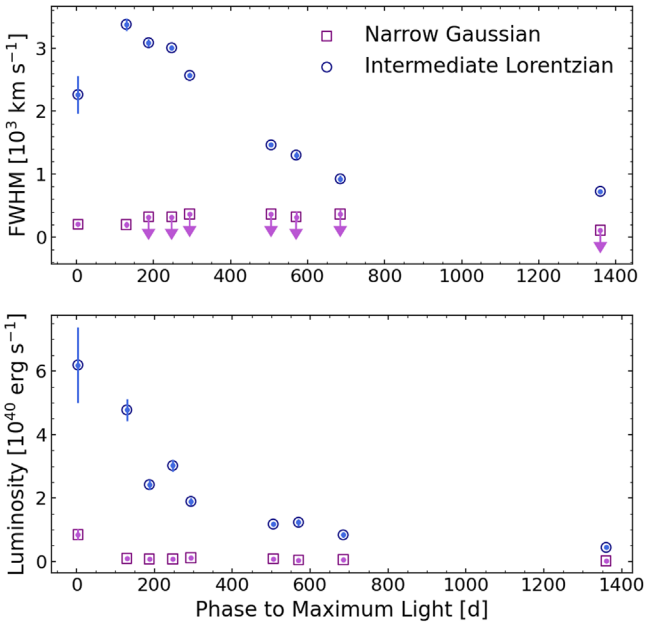

Figure 13. Evolution of the Hα FWHM velocity (top panel) and luminosity (bottom panel). The purple squares are the narrow Gaussian component, while the blue circles are the Lorentzian. The arrows indicate an upper limit for the narrow component, given by the spectral resolution. Phase is in days relative to the *r*-band maximum.

after peak, it is still strongly dominated by emission features of hydrogen, such as it was observed in 2012 for SN 2009ip.

The very late-time optical spectrum of SN 2011fh, obtained on 2015 October 7 at phase +1359 days, is shown in Figure 6. We use `The Atomic Line List v2.04`[17] to identify the emission lines in the spectrum and highlight the main features

[17] https://www.pa.uky.edu/~peter/atomic/

Table 4
FWHM Velocities of the Two Hα Components

Phase (days) (1)	$v_{\rm FWHM,Lorentzian}$ (km s^{-1}) (2)	(1σ error) (3)	$v_{\rm FWHM,Gaussian}$ (km s^{-1}) (4)	(1σ error) (5)
+3	2263.33	299.11	204.03	36.12
+129	3376.06	99.98	197.69	45.53
+187	3087.12	60.19	<320.00	26.19
+246	3006.35	42.37	<320.00	22.12
+293	2568.02	40.41	<365.00	13.23
+505	1464.20	23.71	<365.00	14.67
+570	1302.74	59.22	<320.00	83.59
+684	925.26	56.35	<365.00	68.59
+1359	726.56	14.63	<110.00	12.78

Table 5
Luminosities of the Two Hα Components

Phase (days) (1)	10^{39} $L_{\rm Lorentzian}$ (erg s^{-1}) (2)	(1σ error) (3)	10^{39} $L_{\rm Gaussian}$ (erg s^{-1}) (4)	(1σ error) (5)
+3	61.92	11.94	8.46	1.69
+129	47.75	3.40	0.91	0.23
+187	24.20	1.57	0.77	0.10
+246	30.21	1.89	0.78	0.09
+293	18.90	1.20	1.10	0.09
+505	11.76	0.75	0.83	0.07
+570	12.33	1.08	0.40	0.16
+684	8.36	0.92	0.52	0.19
+1359	4.41	0.29	0.13	0.02

with traced lines. The Fe II emission features (gray traced lines) become very prominent especially near 5200 Å. At this point, the Hα profile is very narrow, being described by a Lorentzian component with $v_{\rm FWHM} \sim 726$ km s^{-1} and a Gaussian component with $v_{\rm FWHM} < 110$ km s^{-1}. The Ca II emission lines also get considerably narrower, with $v_{\rm FWHM} \sim 240$ km s^{-1} for Ca II λ8662 and the two components of the [Ca II] $\lambda\lambda$7291, 7324 doublet. The detected [O II], [O III], and [S II] lines are due most likely to a background H II region and become stronger with time as the contribution from SN 2011fh becomes fainter, while the [O I] lines are probably due to the transient. As shown in Figure 9, we measure a sudden drop in temperature at this epoch, which is not seen for the SUPERBOL measurements in photometry. This difference might be due to the last spectrum being strongly dominated by emission lines, which makes the blackbody fit in the continuum very uncertain. We also fit the Hβ emission lines with intermediate- and narrow-width Lorentzian profiles and use the resultant luminosities to calculate the Balmer decrement evolution. We estimate a relatively low value of Hα/Hβ = 3.01 near peak brightness, which might be due to Case B recombination or a high-density CSM, as it was observed for 2009ip (Levesque et al. 2014). For the phase +246 days, however, we measure Hα/H$\beta \simeq 13$, which is very similar to the value found for the 2009ip–like SN 2016bdu (Pastorello et al. 2017) and other Type IIn SNe (e.g., 1996al; Benetti et al. 2016). Such high ratios might be related to newly formed dust or to Case C recombination where the CSM is optically thick to the Balmer emission lines.

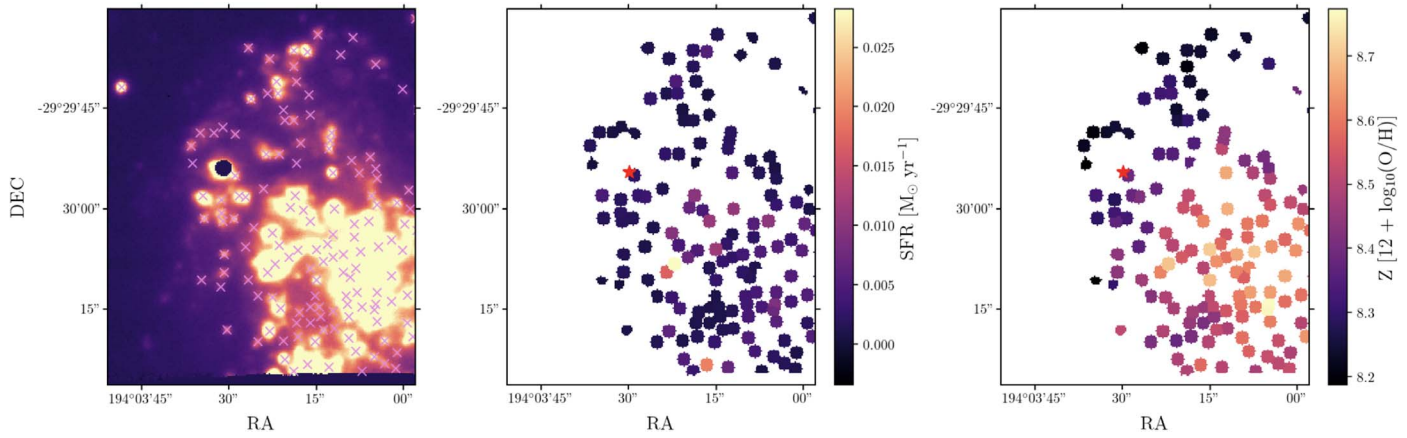

Figure 14. The left panel shows the H II regions selected by `ifuanalysis` superimposed on the Hα emission map. A 6″ region around SN 2011fh was masked to avoid contamination from the SN. The middle panel shows the estimated star formation rate for these regions, in $M_{\odot}$ yr^{-1}, and the right panel shows the metallicity in units of 12 + $\log_{10}$(O/H). In the last two panels, the position of SN 2011fh is marked with a red star.

Table 6
Blackbody Fits to the Spectral Continua

Phase	T_{BB}		10^{41} L_{BB}		10^{14} R_{BB}	
(days)	(K)	(1σ error)	(erg s^{-1})	(1σ error)	(cm)	(1σ error)
(1)	(2)	(3)	(4)	(5)	(6)	(7)
+3	8052	38	34.08	2.17	10.67	0.36
+129	7432	50	5.67	0.38	5.11	0.19
+187	7528	47	2.78	0.18	3.49	0.12
+246	7543	41	4.19	0.27	4.26	0.15
+293	8140	87	2.84	0.22	3.01	0.13
+505	8815	90	2.24	0.17	2.28	0.10
+570	9012	97	1.83	0.13	1.97	0.08
+684	10170	146	1.99	0.16	1.62	0.08
+1359	6942	58	0.65	0.04	1.99	0.08

3.4. Environment Analysis

3.4.1. MUSE Spectroscopy

We use the MUSE data to investigate the H II regions and the environment around SN 2011fh. The datacube was corrected for reddening and redshift using the values from Section 3.1. To avoid contamination from the light of the SN, we masked a 6″ circular region around SN 2011fh. We used `ifuanalysis`[18] to select and estimate the properties of the H II regions. `ifuanalysis` uses `STARLIGHT` (Cid Fernandes et al. 2005; Mateus et al. 2006; Asari et al. 2007) to fit the stellar continuum with stellar population synthesis models and `Astropy` (Astropy Collaboration et al. 2013, 2018) to fit the emission lines with Gaussians.

The H II regions were selected to have a minimum peak Hα flux twice the standard deviation of a region outside of the galaxy, and a maximum spatial size of 5 pixels. In Figure 14, we show the selected regions superimposed on the Hα emission. We also show the estimated oxygen abundances in units of 12 + $\log_{10}$(O/H), based on the calibration of Dopita et al. (2016), and the star formation rate (SFR), estimated using the Hα luminosity as described in Kennicutt (1998), for each H II region. SN 2011fh is located in the outskirts of the galaxy, and the oxygen abundance value of its nearest H II region is 8.39 ± 0.03, or 0.5 $Z_{\odot}$, assuming the solar oxygen abundance of 12 + $\log_{10}$(O/H) = 8.69 (Asplund et al. 2021). This value is surprisingly similar to the metallicity estimated for SN 2009ip by Margutti et al. (2014). The SFR is fairly constant throughout the galaxy, with a median value of $1.8 \times 10^{-3}\,M_{\odot}$ yr^{-1}, although there is one H II region with a high value of $4.8 \times 10^{-2}\,M_{\odot}$ yr^{-1}. SN 2011fh is located near a region with relatively high SFR of $\sim 2.3 \times 10^{-3}\,M_{\odot}$ yr^{-1}.

[18] https://ifuanal.readthedocs.io/en/latest/index.html

3.4.2. HST Analysis

As can be seen in Figure 5, there are a number of bright sources within ∼150 pc of SN 2011fh, probably forming an association with its progenitor star. We used `DOLPHOT` (Dolphin 2016) to perform PSF photometry on these sources using the same selection criteria as described in Section 2.4. We selected a total of 10 stars within a 1″ radius (150 pc) centered in SN 2011fh. The extinction-corrected absolute magnitudes of the stars in the F336W and F814W filters are shown in Table 7.

We used `HOKI` (Stevance et al. 2020a), and its modules `CMD` and `AgeWizard` (Stevance et al. 2020b), to estimate the age of the stellar cluster around SN 2011fh and thus constrain the age of its progenitor. `HOKI` uses stellar population models from Binary Population and Spectral Synthesis (`BPASS`, Eldridge et al. 2017; Stanway & Eldridge 2018).

The selected sources are very blue, which suggests a very young progenitor star for SN 2011fh. In Figure 15, we show the M_{F336W} versus M_{F336W}–M_{F814W} color–magnitude diagram

Table 7
HST Photometry of the Stars around SN 2011fh

F336W		F814W	
(mag) (1)	(error) (2)	(mag) (3)	(error) (4)
−10.57	0.10	−9.30	0.07
−9.10	0.16	−8.63	0.08
−9.23	0.13	−8.23	0.09
−9.52	0.12	−7.73	0.11
−9.19	0.14	−7.83	0.11
−9.13	0.14	−7.73	0.11
−8.46	0.19	−7.83	0.10
−9.10	0.19	−7.38	0.17
−8.33	0.21	−7.49	0.13
−8.35	0.21	−7.26	0.15

of the HST sources, along with the HOKI synthetic CMD. Figure 15 shows that the detected sources are limited to a magnitude of $M_{\rm F336W} \lesssim -8.4$ mag, which affects the detection of fainter sources and places an uncertainty in our analysis. We notice that the crowding of the stars in the region might also affects the detection of sources. We set the metallicity to a value of $0.5\,Z_{\odot}$ and found the best-fitting BPASS model to have an age of $10^{6.7}$ yr. The model was then used in AgeWizard to estimate the probability distribution of ages based on the observed color–magnitude values. The resulting distribution is shown in the bottom panel of Figure 15. The 90% confidence interval spans between $10^{6.4}$ and $10^{6.8}$ yr, with a median value of $10^{6.6}$ yr. This result indicates that the local stellar population, and therefore the progenitor of SN 2011fh, is very young.

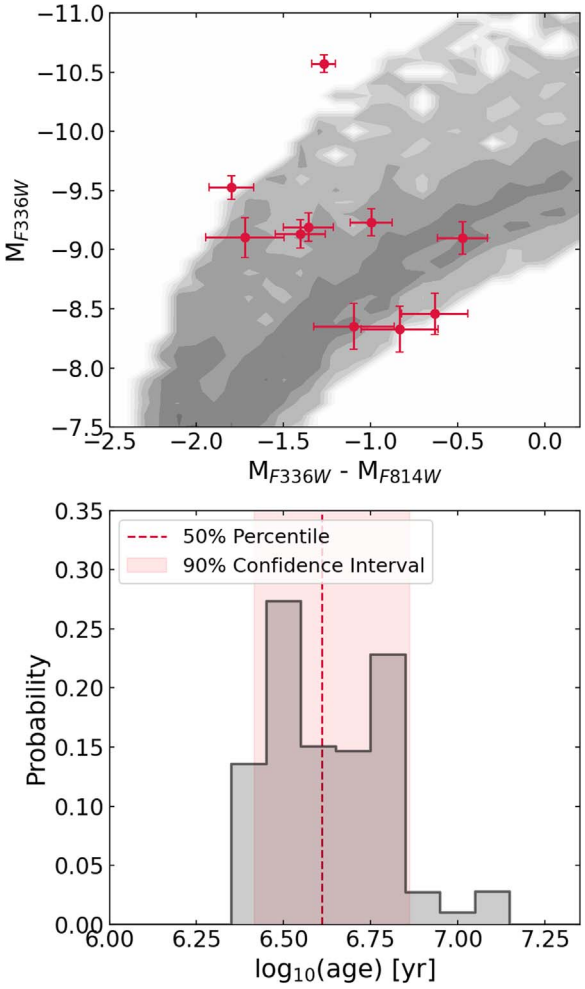

Figure 15. The top panel shows the color–magnitude diagram (CMD) of the bright stars within 1″ (150 pc) of SN 2011fh, along with a HOKI CMD with an age of $10^{6.7}$. The bottom panel shows the AgeWizard probability distribution. The 90% confidence interval of the distribution is highlighted in the red region, and the median is marked as the dashed line.

4. Discussion

The members of the family of SN 2009ip–like transients show remarkable similarities throughout their evolution, which may be indicative of similar progenitors or explosion mechanisms. In Section 4.1, we describe the photometric and spectroscopic similarities of SN 2011fh to SN 2009ip and similar events. We discuss the possibility of dust formation in Section 4.2. We analyze the late-time spectrum of SN 2011fh in Section 4.3, where we also make a parallel with LBV eruptions. The implications of the age estimate for the progenitor star, such as the progenitor mass and possible explosion mechanisms, are discussed in Section 4.4.

4.1. The Relation with SN 2009ip–like Events

As described in Section 3.2 and shown in Figure 7, SN 2011fh, SN 2009ip (Fraser et al. 2013; Mauerhan et al. 2013), SN 2016bdu (Pastorello et al. 2017), and SN 2018cnf (Pastorello et al. 2019b) all show a similar brightening event (Event A) with $M_r \sim -15$ mag ($M_r \sim -16$ mag for SN 2011fh), followed by a luminous outburst (Event B) with $M_r \sim -18$ mag. SN 2009ip had a peak luminosity of $\sim 2 \times 10^{43}$ erg s^{-1} (Mauerhan et al. 2013; Margutti et al. 2014), while SN 2016bdu and SN 2018cnf peaked at $\sim 4 \times 10^{42}$ erg s^{-1} (Pastorello et al. 2017, 2019b) and SN 2011fh at $\sim 3.4 \times 10^{42}$ erg s^{-1} (Figure 9).

The interpretation of the precursor event and its connection to the brighter one is still unclear, with ideas ranging from an explosion (faint core collapse or a major outburst in a massive star) followed by ejecta–CSM interaction (Moriya 2015; Elias-Rosa et al. 2016; Pastorello et al. 2017), an outburst preceding an SN (Ofek et al. 2013; Pastorello et al. 2017), or the result of binary interactions (Kashi et al. 2013; Levesque et al. 2014; Goranskij et al. 2016). The slow brightening seen for SN 2011fh in the months before peak might indicate an LBV-like eruptive state shortly before a major outburst, as it is commonly observed for SN impostors (Smith et al. 2011), or even Type IIn SNe (Ofek et al. 2014; Strotjohann et al. 2021). The mechanism behind Event B, in this case, could be either the shock generated by a real core collapse of the progenitor star or some energetic eruption originating in instabilities that are thought to operate in massive stars, such as pulsational pair instability (Woosley et al. 2007), unsteady burning, or interaction with other stars (Smith 2014; Smith & Arnett 2014). We cannot rule out the possibility that the first brightening was in fact the main explosive event and that the following event was generated by its shock interacting with CSM shells. This scenario was invoked by Pastorello et al. (2017) in the case of SN 2016bdu and by Elias-Rosa et al. (2016) for SN 2015bh. Moriya (2015) described a similar scenario in which the Event B observed in SN 2009ip was generated by shell–shell collisions. Unfortunately, the slow brightening event of SN

2011fh was only observed in the r band, and the lack of other colors or spectroscopic observations during this period makes it hard to constrain its true nature.

Prediscovery images of SN 2009ip and SN 2016bdu have shown LBV-like variability for their progenitors, with observed outbursts reaching $M_r \sim -14$ mag (Mauerhan et al. 2013; Pastorello et al. 2017). In Figure 2 we have shown that nearly five years before the luminous outburst of 2011 the source ranged between $M_r \sim -14.5$ mag and $M_r \sim -15.5$ mag. We note, however, that these observations are relatively shallow, and these oscillations might not be real. For this reason, it is not possible to conclude if such behavior is related to a physical process in the progenitor star.

In the days following peak brightness, SN 2009ip, SN 2016bdu, and SN 2018cnf all show a very similar "shoulder" in their light curve (see Figure 7), probably caused by a collision between CSM shells (Fraser et al. 2013; Mauerhan et al. 2013; Pastorello et al. 2017, 2019b). Although photometry of SN 2011fh is not available at this period, bumps in its r-band light curve are seen at ∼228 and ∼350 days after peak, probably generated by the same mechanism. The late-time brightness evolution of SN 2009ip and SN 2016bdu is very slow, probably due to ongoing interaction with a dense CSM (Graham et al. 2017; Pastorello et al. 2017). SN 2011fh also shows a slow evolution at later times, with an apparent flattening of the light curve after 2014. The 2016 October 20 HST observations revealed a source with an absolute magnitude of $M_{\rm F814W} \approx -13.32$ at the position of SN 2011fh. This is more luminous than the expected for a star in a quiescent stage, which might suggest that the progenitor star is going through an LBV-like eruptive state. However, emission due to continuous interaction between the ejecta and the CSM is a common mechanism used to explain late-time emission of Type IIn SNe and other interacting transients (Taddia et al. 2013; Fraser 2020) and might explain this late-time emission for SN 2011fh.

Besides their photometric correspondences, SN 2009ip–like events also show remarkable similarities in their spectroscopic evolution. In Figure 16, we show the comparison of the spectral evolution of SN 2011fh to SN 2009ip (Fraser et al. 2013; Margutti et al. 2014; Fraser et al. 2015; Graham et al. 2017), SN 2016bdu (Pastorello et al. 2017), and SN 2018cnf (Pastorello et al. 2019b). The four objects are very similar near peak brightness, with blue continua and prominent narrow- to intermediate-width Balmer emission features. SN 2011fh and SN 2018cnf, however, have lower blackbody temperatures, with a measured $\sim 8.3 \times 10^3$ K for the latter, while SN 2009ip and SN 2016bdu show temperatures of $\sim 1.2 \times 10^4$ K and $\sim 1.7 \times 10^4$ K, respectively (Graham et al. 2014; Pastorello et al. 2017).

At +129 days, SN 2011fh has a very distinctive P Cygni absorption feature, which indicates the presence of fast-moving material at ∼6400 km s^{-1}. A similar feature with a velocity of ∼5000 km s^{-1} was seen for SN 2009ip at similar epochs (Margutti et al. 2014). At +78 days, SN 2016bdu also shows a prominent absorption feature at ∼3800 km s^{-1} (Pastorello et al. 2017). We note that higher-velocity components were detected for both transients at earlier epochs, with measured FWHM values of up to ∼13,000 km s^{-1} (Margutti et al. 2014; Pastorello et al. 2017). Another SN 2009ip–like event, LSQ 13zm, presented even higher measured velocities of up to ∼22,000 km s^{-1} (Tartaglia et al. 2016).

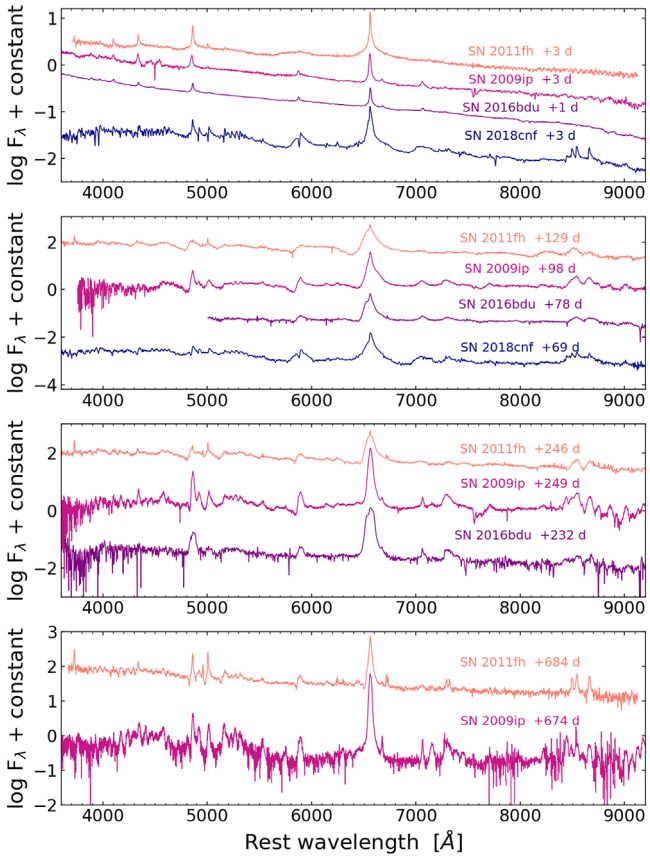

Figure 16. Spectral comparison of SN 2011fh to SN 2009ip (Fraser et al. 2013; Margutti et al. 2014; Fraser et al. 2015; Graham et al. 2017), SN 2016bdu (Pastorello et al. 2017), and SN 2018cnf (Pastorello et al. 2019b) at peak brightness and near phases ∼100, 240, and 680 days.

For spherical symmetry, it is possible to estimate the mass-loss rate of the progenitor star assuming that ejecta–CSM shock interaction powers the light curve (e.g., Smith 2013). Using the CSM luminosity, $L_{\rm CSM}$, the velocity of the cold dense shell, $V_{\rm CDS}$, and the velocity of the unshocked CSM, $V_{\rm CSM}$, and assuming 100% efficiency of converting shock kinetic energy into radiation,

$$\dot{M} = 2\, L_{\rm CSM}\, \frac{V_{\rm CSM}}{V_{\rm CDS}^3}. \quad (1)$$

Using $V_{\rm CDS} \approx 3000$ km s^{-1}, $V_{\rm CSM} \approx 100$ km s^{-1}, and $L_{\rm CSM} \simeq L_{\rm peak} \approx 3 \times 10^{42}$ erg s^{-1}, we get $\dot{M} \sim 4 \times 10^{-2}\, M_\odot$ yr^{-1}. This value is fully consistent with the estimated mass-loss rate for the progenitor of SN 2009ip of $\sim 10^{-2}$–$10^{-1}\, M_\odot$ yr^{-1} (Fraser et al. 2013; Margutti et al. 2014). The observed mass-loss rate of SN 2011fh also falls within the observed range of mass-loss rates for Type IIn SNe of 10^{-2}–$10^{-1}\, M_\odot$ yr^{-1} (Kiewe et al. 2012) and 10^{-4}–$10^{-2}\, M_\odot$ yr^{-1} (Taddia et al. 2013).

As noted by Brennan et al. (2021a), 2009ip–like transients often show asymmetries in their Hα emission profile. The line in AT 2016jbu was very asymmetric, in SN 2009ip it was very symmetric, and in SN 2016bdu it was somewhat asymmetric. SN 2011fh shows a degree of Hα symmetry somewhat similar to SN 2016bdu, with a clearly asymmetrical shape until phase +293 (See Figure 3 and Figure 12). This behavior of the Hα profile might be related to asymmetries in the CSM.

At late times (∼240 days after peak), SN 2011fh, SN 2009ip, and SN 2016bdu are still dominated by emission lines of H and He, which indicates the ongoing interaction with a dense CSM. All three objects show Ca II emission at this phase, and both SN 2009ip and SN 2016bdu show He I λ7065 emission, which will develop later in SN 2011fh. The Fe emission-line forest is also visible for the three events and is particularly strong for SN 2009ip. Pastorello et al. (2017) noted that SN 2016bdu shows nebular lines of [O I] at this epoch and that those lines are expected for core-collapse SNe. The same was true for SN 2011fh. Although differing in some details, the Hα profile of all the three events around this epoch can be described by a narrow feature superimposed on an intermediate-width feature.

As noted by Graham et al. (2017) for SN 2009ip, SN 2011fh also shows a distinctive O I λ8446 emission line but no O I λ7774 at very late times. This suggests that O I λ8446 is being created by Bowen Lyβ fluorescence, which is consistent with a very dense and optically thick medium. Fraser et al. (2015) showed that SN 2009ip had a ratio of the intensity of the [O I] $\lambda\lambda$6300, 6363 lines of ∼1. Although this ratio suggests newly synthesized oxygen in the ejecta, Fraser et al. (2015) argue that the lack of evolution of this value points toward the presence of primordial oxygen. We note a very similar scenario for SN 2011fh, which has a ratio of 0.9 ± 0.3 at the phase of +684 days and 1.6 ± 0.3 at +1359 days. As seen in Figure 16, SN 2011fh and SN 2009ip also show other similarities at phase ∼+680 days, such as the presence of strong Ca II features and the Fe II emission-line forest. The Hα/Hβ flux ratio for SN 2009ip of around 40 at this epoch is very high (Graham et al. 2017), while we estimate Hα/H$\beta \approx 7$ for SN 2011fh.

4.2. The Presence of Dust

In Section 3.2.2, we found that the SED of SN 2011fh has a significant IR excess that can be described by dust emission with a temperature of ∼950 K at phase +570 days and ∼1116 K at phase +1143 days.

The dust emission is located at $\sim 10^{16.52}$ cm at phase +570 and decreases to $\sim 10^{16.44}$ cm at later epochs (see Table 3). Dust emission is quite common for interacting transients (Prieto et al. 2008; Berger et al. 2009; Foley et al. 2011; Fox et al. 2011), but distinguishing between preexisting or newly formed dust is not easy. SN 2011fh shows a similar mid-IR color evolution to several Type IIn SNe and other interacting transients, such as SN 2009ip (Szalai et al. 2021). Asymmetries in the Hα caused by the suppression of the red wing relative to the blue wing are often used as an indicator for the detection of newly formed dust (e.g., Fox et al. 2011). Although SN 2011fh has small asymmetries, it is hard to conclude whether it is caused by dust formed in the luminous outburst. The dust inner radius of $\sim 10^{16.5}$ cm is larger than the photospheric radius of $\sim 10^{14}$ cm. This indicates that dust is expanding slowly, if at all, and shows little optical depth evolution, all of which suggests that dust is preexisting.

The dust mass is

$$M_{\rm dust} = \frac{4\pi\tau_V R_{\rm dust}^2}{\kappa_V}, \quad (2)$$

where $\kappa_V \approx 2000\ {\rm cm^2\ g^{-1}}$ is the visual opacity for silicate dust (Fox et al. 2010). Using the properties estimated at +570 days, we get $\sim 2 \times 10^{-3}\ M_\odot$. For a typical gas to dust mass ratio of ∼100, the total mass associated with the dust shell is $\sim 0.2\ M_\odot$.

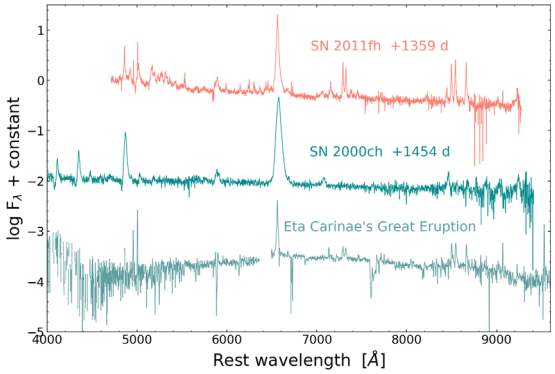

Figure 17. Spectral comparison of the very late-time spectrum of SN 2011fh, taken 1359 days after peak, to the spectrum of SN 2000ch at a similar phase (Smith et al. 2011). We also show the light-echo spectrum of the Great Eruption of Eta Carinae (Smith et al. 2018a).

These values are much larger than were estimated for the LBV outburst UGC 2773 OT2009-1 (Foley et al. 2011) and for the SN 2009ip–like event AT 2016jbu (Brennan et al. 2021a, 2021b) but fall well within the range of dust masses estimated for Type IIn SNe by Fox et al. (2011).

4.3. The Late-time Spectrum

Type IIn SNe often show spectra dominated by Balmer lines in emission until very late periods, instead of the nebular lines of heavy elements seen in noninteracting SNe. Some known exceptions are SN 1998S, which showed emission lines of [O I] and [Ca II] in the years after the explosion (Leonard et al. 2000), and SN 1995N, where nebular lines of [O I], [O II], and [O III] appeared at very late times (Fransson et al. 2002). As was shown by Taddia et al. (2013), Type IIn SNe can show Hα features with velocities of $\sim 10^4\ {\rm km\ s^{-1}}$ and luminosities between 10^{40} and $10^{41}\ {\rm erg\ s^{-1}}$ up to 180 days after peak. The spectra of SN impostors are also dominated by Balmer lines at late times, and many show Ca II emission lines (Smith et al. 2011). One example is SN 2000ch, which reached $M_R \sim -12.8$ mag (Wagner et al. 2004) and had broad lines of Hα with FWHM velocities of $\sim 1500\ {\rm km\ s^{-1}}$ (Smith et al. 2011).

As described in Section 3.3, the very late-time spectrum of SN 2011fh shows prominent lines of Fe II, Ca II, O I, and He I, while still being dominated by strong Balmer features. The Hα profile at this epoch shows an intermediate-width component with a FWHM velocity of $\sim 726\ {\rm km\ s^{-1}}$, and a luminosity of $\sim 4 \times 10^{39}\ {\rm erg\ s^{-1}}$.

Although it is hard to determine whether SN 2011fh was a terminal event, we note several similarities between its late-time spectrum and those of SN impostors. In Figure 17, we compare the spectrum of SN 2011fh to SN 2000ch at phase +1454 days (Smith et al. 2011) and to the 19th century Great Eruption of the Galactic LBV star Eta Carinae (Smith et al. 2018a). SN 2011fh and SN 2000ch are both dominated by narrow- to intermediate-width Balmer lines in emission until very late periods, with some He I features. The continuum slopes of the two spectra are very similar, indicating a similar photospheric temperature. SN 2000ch also shows a prominent O I λ8446 emission line, which is also present in SN 2011fh. Although SN 2000ch does not show the strong Ca II features seen in SN 2011fh, these lines are present in the spectra of Eta Carinae's Great Eruption (Smith et al. 2018a) and are strong features in the spectra of some events arising from lower-mass

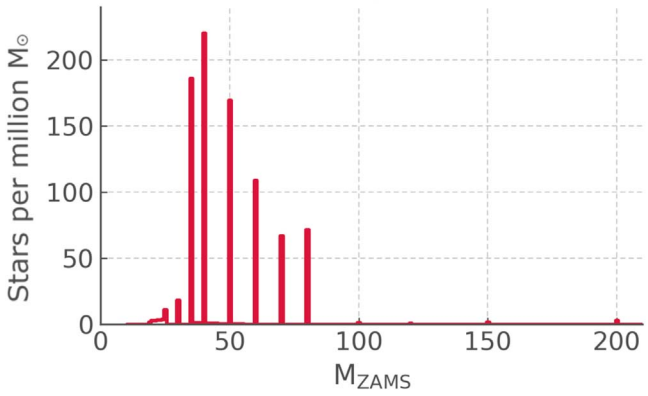

Figure 18. Number of stars per million $M_{\odot}$ obtained using BPASS. The discrete number of ZAMS masses come from the grid of initial masses used in the BPASS models. The highest bars in the distribution extend between 35 and 80 $M_{\odot}$.

progenitors, such as SN 2008S (Botticella et al. 2009; Smith et al. 2009), NGC 300-OT (Berger et al. 2009; Bond et al. 2009), and SN 2002bu (Smith et al. 2011). We note that SN 2002bu and SN 2008S are sometimes referred to as intermediate-luminosity red transients (ILRTs) and that many studies support the scenario of SN 2008S–like events being terminal SN explosions (Botticella et al. 2009; Adams et al. 2016; Cai et al. 2021). The late-time spectrum of SN 2011fh also shows strong similarities with the spectra of UGC 2773 OT2009-1 (Smith et al. 2010; Foley et al. 2011), an analog to Eta Carinae's Great Eruption (Smith et al. 2016b).

After peak, SN 2000ch remained in a plateau at ~ -10.6 mag, which could have been the quiescent magnitude of the progenitor star or an S-Dor–like eruptive state (Wagner et al. 2004; Smith et al. 2011). Pastorello et al. (2010) described in detail two other bright eruptions related to the star, in 2008 and 2009, when it reached ~ -12.8 during the brightest one. Pastorello et al. (2010) noted many observational similarities with the system HD 5980, which is a binary consisting of an erupting LBV and a Wolf-Rayet star, and suggested binary interactions as an explanation for the variability and eruptions detected for SN 2000ch. A similar scenario is often used to explain the Great Eruption of Eta Carinae.

4.4. Implications of the Progenitor Age and Mass

Our estimates of the age of the stars around SN 2011fh indicate that the progenitor is a very young star with ~4.5 Myr. Using $0.5\,Z_{\odot}$ and a 4.5 Myr MIST (Paxton et al. 2011, 2013, 2015, 2018) single-star isochrone, we get a maximum mass of $\sim 60\,M_{\odot}$. Because the fraction of binary systems is very high at large stellar masses, we also use BPASS (Eldridge et al. 2017; Stanway & Eldridge 2018) to estimate the progenitor mass. Using the age distribution of 2–6 Myr (see Figure 15), a half-solar metallicity, and after selecting progenitors that could result in neutron star remnants with $<2.5\,M_{\odot}$ (based on Figure 3 of Abbott et al. 2018) and cutting out pulsational pair-instability candidates that reached a He core mass of $>40\,M_{\odot}$, we obtained the distribution of the number of stars per million solar masses as a function of their ZAMS mass, as shown in Figure 18. The discrete number of ZAMS masses presented in Figure 18 is a consequence of the grid of initial masses used in the BPASS models (see Eldridge et al. 2017). The distribution shows that there is a large number of stars populating the 35–80 $M_{\odot}$ mass range, with the three tallest bars being between 35 and 50 $M_{\odot}$. We note, however, that an energetic outburst such as SN 2011fh would be more likely to occur with stars in the most massive half of the distribution, even though the relative number of stars is slightly lower than the less massive half. The $\sim 60\,M_{\odot}$, obtained by single-star models, and the 35–80 $M_{\odot}$ range, obtained considering binary systems, are surprisingly similar to the estimates of 50–80 $M_{\odot}$ (Smith et al. 2010) and of $\gtrsim 60\,M_{\odot}$ (Foley et al. 2011) for SN 2009ip. It also agrees well with the results of Pastorello et al. (2019b), who showed that the progenitor of SN 2018cnf was consistent with a massive hypergiant or an LBV. We note that our results contrast with the estimates of Brennan et al. (2021a, 2021b), who showed that the progenitor of AT 2016jbu was a relatively less massive hypergiant star with $\sim 20\,M_{\odot}$. This might indicate that this type of event can be originated by progenitors with a large range of initial masses.

One common factor used to explain instabilities in LBV stars is their proximity to the classical Eddington limit, which would help to create strong winds. Eta Carinae is thought to have exceeded the Eddington limit by a factor of ~5 during its Great Eruption (Smith et al. 2018a). We estimate a still larger Eddington factor of ~30 for SN 2011fh at the beginning of the brightening event of February of 2011, when it had a magnitude of $M_r \approx -15.2$. An Eddington factor of ~100 is reached at the end of this period, just before the luminous outburst of August 2011.

Super-Eddington winds can arise from energy deposited in the envelope of massive stars by different mechanisms, including wave heating and unstable fusion (Quataert & Shiode 2012; Shiode & Quataert 2014; Quataert et al. 2016). Binary interactions may also be a mechanism for injecting energy into the outer layers of a massive star because more than half of all massive stars are in binary systems with short-enough periods to generate some kind of interaction or collision (Sana et al. 2012; Smith 2014). The interactions typically begin when the more massive star evolves off the main sequence. This is a scenario often used to explain the behavior of Eta Carinae (Smith & Frew 2011; Smith et al. 2018a).

The pulsational pair-instability mechanism is capable of explaining the extreme mass loss seen in LBV stars (Woosley et al. 2007) and was considered as an explanation for SN 2009ip by Pastorello et al. (2013), Mauerhan et al. (2013), and Fraser et al. (2013). Margutti et al. (2014), however, demonstrated that, for a mass limit of 85 $M_{\odot}$ and a metallicity of 0.4–0.9 $Z_{\odot}$, the progenitor of SN 2009ip would have a helium-core mass lower than the ~40 $M_{\odot}$ needed for a pulsational pair instability. Because SN 2011fh is so similar to SN 2009ip, the pulsational pair instability seems to be an unlikely mechanism for its bright eruptions.

Finally, we cannot fully exclude the possibility of SN 2011fh being a weak SN, although this appears less likely. Under-energetic explosions arising from core collapse are expected to occur in such massive stars (Heger et al. 2003; Moriya et al. 2010; Sukhbold et al. 2016). Mauerhan et al. (2013) used this mechanism to explain the double-peaked light curve of SN 2009ip, where Event A would be a weak core-collapse event and Event B would be powered by the ejecta shock interacting with a dense CSM. Smith et al. (2014) noted a similarity of the Event A of SN 2009ip to SN 1987A, an SN generated by a blue

supergiant star (Arnett et al. 1989). A similar statement was made by Elias-Rosa et al. (2016) in the case of SN 2015bh. Pastorello et al. (2017) showed that other SN 2009ip–like events, such as SN 2016bdu, SN 2010mc (Smith et al. 2014), and LSQ 13zm (Tartaglia et al. 2016), have Event A light curves that are very similar to the faint SN 1987A–like SN 2009E (Pastorello et al. 2012). SN 2011fh, however, does not appear to present such similarities.

5. Conclusion

In this paper, we presented optical, near-infrared, and infrared observations of the Type IIn SN 2011fh, spanning from 2007 to 2017. The results can be summarized as follows:

1. SN 2011fh shows several similarities to the peculiar SN 2009ip and similar transients, such as SN 2016bdu and SN 2018cnf. They include(1) an initial spectral resemblance to typical Type IIn SNe, with a blue continuum and narrow- to intermediate-width Balmer emission lines; (2) a brightening event that lasts ∼5 months and reaches $M_r \sim -16$ mag, followed by a luminous outburst with $M_r \sim -18$ mag at peak; (3) a very similar light curve, with bumps and a slow fading with time; and (4) a very similar spectroscopic evolution, with signals of CSM interaction until very late times, distinctive P Cygni features indicating a fast-moving material, and the presence of Ca II and Fe II lines.
2. The estimated progenitor mass-loss rate of $\sim 4 \times 10^{-2}\, M_\odot\ \mathrm{yr}^{-1}$ is consistent with mass-loss rate estimates for SN 2009ip and Type IIn SNe.
3. SN 2011fh shows a significant IR excess that can be described by warm dust emission with $T_{\rm dust} \approx 1000$ K and $R_{\rm dust} \approx 3 \times 10^{16}$ cm. The emission was probably created by preexisting dust with a mass of $M_{\rm dust} \sim 2 \times 10^{-3}\, M_\odot$.
4. The very late-time spectrum of SN 2011fh shows strong similarities to some SN impostors observed at the same phase. The detection of narrow Ca II features and Balmer emission lines is also similar to the Great Eruption of Eta Carinae.
5. SN 2011fh is located in a region with relatively rapid star formation ($\sim 2 \times 10^{-3}\, M_\odot\ \mathrm{yr}^{-1}$). The H II region oxygen abundance of $12 + \log(\mathrm{O/H}) = 8.39$ ($\sim 0.5\, Z_\odot$) is similar to what was estimated at the location of SN 2009ip.
6. The local stellar population has an age of ∼4.5 Myr, which corresponds to a progenitor with an initial main-sequence mass of $\sim 60\, M_\odot$, if we consider a single-stellar evolution model, or a range of 35–80 $M_\odot$, considering binary systems. These mass estimates are similar to the estimates for SN 2009ip's progenitor, and consistent with very massive stars passing through the LBV phase.
7. SN 2011fh exceeded the classical Eddington limit by a large factor in the months before the luminous outburst of 2011. This suggests that a possible mechanism behind the bright event is related to strong supper-Eddington winds.

Although SN 2011fh shows striking similarities with both impostors and 2009ip–like events, it is hard to conclude whether SN 2011fh was a genuine core-collapse SN or a nonterminal event where the mass recently ejected collides with preexisting CSM and generates a luminous outburst. The lack of observational signatures related to a core collapse, such as broad Balmer and O I lines at late times, makes the scenario of a true SN less likely. Our results therefore imply that at least a fraction of SN 2009ip–like events arise from nonterminal eruptions in massive and young stars. The discovery and follow-up observations of new transients similar to SN 2009ip will certainly help in the understanding of the mechanisms behind this unique class of events.

We would like to thank Andrea Pastorello and Melissa Graham for kindly sharing their data on SN 2016bdu, SN 2018cnf, and SN 2009ip. We thank the Carnegie Supernova Project-II for obtaining several photometric observations presented in the paper, and in particular Carlos Contreras, Mark Phillips, Nidia Morrell, and Eric Hsiao. T.P. is supported by CONICYT's Programa de Astronomía through the ALMA-CONICYT 2019 grant 31190017. Support for J.L.P. is provided in part by ANID through the Fondecyt regular grant 1191038 and through the Millennium Science Initiative grant ICN12_09, awarded to The Millennium Institute of Astrophysics, MAS. C.S.K. is supported by NSF grants AST-1814440 and AST-1907570. HFS acknowledges the support of the Marsden Fund Council managed through Royal Society Te Aparangi. This paper includes optical and NIR photometry obtained by the Carnegie Supernova Project, which was generously supported by NSF grants AST-1008343, AST-1613426, AST-1613455, and AST-1613472.

Software: HOKI (Stevance et al. 2020a, 2020b), BPASS (Eldridge et al. 2017; Stanway & Eldridge 2018), FIREHOSE (Simcoe et al. 2013), IRAF (Tody 1986, 1993), Astropy (Astropy Collaboration et al. 2013, 2018), Photutils (Bradley et al. 2019), PYPHOT (https://mfouesneau.github.io/docs/pyphot/), DUSTY (Ivezic & Elitzur 1997), DOLPHOT (Dolphin 2016), SUPERBOL (Version 1.7; Nicholl 2018), ifuanalysis (https://ifuanal.readthedocs.io/en/latest/index.html), STARLIGHT (Cid Fernandes et al. 2005; Mateus et al. 2006; Asari et al. 2007).

Appendix A
Contamination

SN 2011fh is located in a relatively crowded region of the NGC 4806 galaxy, with several bright stars in the proximity (see Figure 5). These stars lie within 150 pc (1″) around SN 2011fh, with several brighter sources within 300 pc (2″). Because the pixel scale of the pre-SN observations were limited up to 2″, we decided to estimate the possible contamination of the stellar cluster to our photometric measurements.

To quantify the amount of contamination in the optical bands, we first performed aperture photometry of the stars around SN 2011fh in the HST F336W and F814W images, using the `Astropy` (Astropy Collaboration et al. 2013, 2018) package `Photutils` (Bradley et al. 2019) in a 2″ region. After subtracting the flux of SN 2011fh, we obtained a contribution from the stars in this aperture of 20.67 and 20.05 mag in the F336W and F814W filters, respectively. By assuming a flat spectrum for the stellar cluster, we then interpolated between the F336W and F814W filter fluxes and performed synthetic photometry in the resulting line with `PYPHOT`[19] to obtain the estimates of $V \approx 20.17$, $r \approx 20.18$, and $i \approx 20.18$. If we compare these values with the PSF photometry of SN 2011fh presented in Tables 8 and 9, the estimated contribution from the cluster is significantly lower than the flux of SN 2011fh throughout its photometric evolution.

[19] https://mfouesneau.github.io/docs/pyphot/

Table 8
Amateur Astronomers' Data and the CRTS *r*-band Photometry of SN 2011fh

UT Date	JD	r	
		(mag)	(error)
(1)	(2)	(3)	(4)
2007-1-25	2,454,126.20298	17.879	0.12
2007-2-22	2,454,154.20024	17.988	0.13
2007-3-9	2,454,169.17404	18.272	0.178
2007-3-27	2,454,187.19841	17.961	0.125
2007-4-6	2,454,197.17815	18.547	0.25
2007-4-16	2,454,207.0734	18.184	0.16
2007-5-7	2,454,228.04447	18.278	0.177
2007-5-14	2,454,235.05647	18.097	0.143
2007-6-16	2,454,267.97322	17.943	0.131
2007-7-4	2,454,285.85462	17.999	0.134
2007-7-20	2,454,301.85781	18.232	0.166
2007-8-12	2,454,324.88361	17.985	0.129
2007-12-28	2,454,463.18063	18.09	0.136
2008-1-22	2,454,488.1978	18.273	0.182
2008-2-7	2,454,504.25914	18.057	0.135
2008-2-8	2,454,505.25765	18.121	0.148
2008-2-29	2,454,526.17647	17.988	0.135
2008-3-11	2,454,537.18612	18.286	0.179
2008-5-6	2,454,593.06685	17.937	0.127
2008-5-11	2,454,598.10991	17.912	0.131
2008-5-28	2,454,615.0704	18.239	0.179
2008-6-27	2,454,644.9809	17.992	0.14
2008-12-31	2,454,832.20995	18.118	0.15
2009-1-5	2,454,837.49042	18.121	0.243
2009-2-25	2,454,888.21891	18.207	0.165
2009-3-15	2,454,906.27249	17.734	0.106
2009-3-27	2,454,918.21621	17.877	0.127
2009-4-15	2,454,937.1613	18.235	0.172
2009-4-27	2,454,949.13822	17.857	0.11
2009-4-29	2,454,951.09237	17.945	0.138
2009-5-11	2,454,963.0813	18.071	0.156
2009-5-12	2,454,964.30533	17.799	0.163
2009-5-29	2,454,981.11436	17.79	0.126
2009-6-19	2,455,002.00408	18.2	0.164
2009-7-18	2,455,030.93214	18.241	0.166
2010-1-21	2,455,218.17694	17.777	0.101
2010-2-21	2,455,249.13263	18.289	0.171
2010-3-9	2,455,265.12761	17.893	0.118
2010-4-8	2,455,295.17376	18.055	0.131
2010-4-17	2,455,304.11246	18.077	0.144
2010-5-10	2,455,327.01388	17.666	0.091
2010-5-22	2,455,339.01684	17.92	0.118
2010-6-13	2,455,361.0242	17.762	0.107
2010-6-30	2,455,378.24321	17.948	0.189
2010-7-16	2,455,393.9443	17.752	0.118
2010-7-22	2,455,399.93913	17.83	0.112
2010-7-28	2,455,406.20502	17.969	0.2
2011-2-11	2,455,603.5911	17.636	0.146
2011-2-24	2,455,617.25406	17.216	0.061
2011-2-24	2,455,617.4946	17.549	0.102
2011-4-13	2,455,665.05019	17.037	0.054
2011-4-24	2,455,676.10863	17.176	0.063
2011-4-25	2,455,677.4096	17.271	0.098
2011-5-9	2,455,691.0465	16.845	0.052
2011-5-26	2,455,708.02969	16.936	0.053
2011-6-2	2,455,715.3151	16.716	0.075
2011-6-3	2,455,716.22604	16.883	0.072
2011-6-16	2,455,728.86432	16.855	0.089
2011-6-21	2,455,734.03201	16.671	0.073
2011-6-27	2,455,739.96366	16.694	0.045

Table 8
(Continued)

UT Date	JD	r	
		(mag)	(error)
(1)	(2)	(3)	(4)
2011-6-28	2,455,741.29443	16.799	0.067
2011-6-30	2,455,742.91587	16.861	0.057
2011-6-30	2,455,742.91587	16.837	0.058
2011-7-17	2,455,759.84951	16.614	0.048
2011-7-28	2,455,770.90473	16.264	0.036
2011-8-2	2,455,776.20691	16.342	0.068
2011-8-9	2,455,782.84013	15.726	0.037
2011-8-24	2,455,798.24181	14.942	0.028
2011-8-25	2,455,799.24933	14.962	0.029
2011-9-4	2,455,809.21792	15.362	0.031
2011-9-5	2,455,810.22498	15.321	0.033
2011-12-16	2,455,911.57505	16.731	0.046
2011-12-25	2,455,920.58029	16.704	0.041
2012-1-6	2,455,932.58682	16.748	0.041
2012-1-25	2,455,951.5711	17.092	0.051
2012-1-28	2,455,954.56738	17.373	0.06
2012-2-16	2,455,973.54651	17.275	0.061
2012-2-17	2,455,975.08906	17.701	0.151
2012-2-24	2,455,981.55593	17.543	0.078
2012-3-25	2,456,012.45263	17.469	0.068
2012-3-30	2,456,017.15598	17.379	0.073
2012-4-10	2,456,028.43419	16.886	0.047
2012-4-11	2,456,029.14365	16.912	0.055
2012-4-19	2,456,037.0854	17.121	0.062
2012-5-15	2,456,063.026	17.33	0.073
2012-7-8	2,456,116.95661	17.984	0.21
2012-8-12	2,456,151.87688	17.671	0.104
2012-8-12	2,456,152.21301	17.248	0.063
2012-12-17	2,456,278.54791	18.305	0.173
2012-12-21	2,456,282.56931	18.225	0.167
2013-1-1	2,456,294.20582	18.136	0.154
2013-1-22	2,456,314.55775	18.103	0.183
2013-2-7	2,456,330.57937	17.952	0.106
2013-2-18	2,456,341.58446	18.258	0.161
2013-2-21	2,456,344.5748	18.055	0.124
2013-2-24	2,456,348.40002	18.19	0.236
2013-3-2	2,456,354.49434	18.059	0.203
2013-3-9	2,456,361.45919	17.904	0.164
2013-3-17	2,456,368.53775	18.08	0.164
2013-4-11	2,456,394.39371	18.169	0.142
2013-4-19	2,456,402.41645	17.842	0.106
2013-4-30	2,456,413.32136	18.037	0.134
2013-5-1	2,456,414.3878	18.168	0.167
2013-5-2	2,456,415.27285	18.079	0.152
2013-5-4	2,456,417.32889	18.428	0.221
2013-5-5	2,456,418.36387	18.204	0.146
2013-5-10	2,456,423.27335	17.848	0.117
2013-5-11	2,456,424.21595	18.38	0.201
2013-5-12	2,456,425.26083	17.842	0.098
2013-5-14	2,456,427.23059	18.231	0.178
2013-5-16	2,456,429.43702	18.163	0.146
2013-5-31	2,456,444.31843	18.282	0.171
2013-6-3	2,456,447.31712	18.319	0.173
2013-6-5	2,456,449.28426	18.329	0.169
2013-6-15	2,456,459.21472	18.617	0.289
2013-6-16	2,456,460.28568	18.334	0.193
2013-6-26	2,456,470.25602	18.18	0.15
2013-6-28	2,456,472.28668	18.422	0.194
2013-6-29	2,456,473.2751	17.967	0.108

Table 9
BVri-CSP2 Photometry of SN 2011fh

UT Date	JD	*B*		*V*		*r*		*i*	
		(mag)	(error)	(mag)	(error)	(mag)	(error)	(mag)	(error)
(1)	(2)	(3)	(4)	(5)	(6)	(7)	(8)	(9)	(10)
2013-2-20	2,456,343.85	18.843	0.0215	18.493	0.0173	18.063	0.0132	18.4135	0.0151
2013-3-3	2,456,354.78	18.8695	0.0226	18.5055	0.0193	18.0805	0.0142	18.41	0.0185
2013-3-15	2,456,366.71	18.9345	0.0244	18.576	0.0193	18.1375	0.0154	18.5	0.0202
2013-3-18	2,456,369.91	…	…	…	…	18.15	0.0155	18.407	0.0324
2013-3-25	2,456,376.76	…	…	…	…	18.155	0.0146	18.529	0.0213
2013-4-5	2,456,387.68	18.913	0.0193	18.573	0.0195	18.1565	0.0132	18.525	0.0171
2013-4-20	2,456,402.73	18.962	0.0265	18.5725	0.0244	18.193	0.0182	18.522	0.0324
2013-5-4	2,456,416.68	19.1855	0.0273	18.8505	0.0245	18.1565	0.0132	18.816	0.0232
2013-5-12	2,456,424.75	19.103	0.0233	18.795	0.0243	18.3765	0.0151	18.795	0.0251
2013-6-1	2,456,444.68	19.046	0.0254	…	…	18.341	0.0192	18.717	0.0291
2015-3-16	2,457,097.76	19.7675	0.0205	19.559	0.0165	18.341	0.0192	19.558	0.0177
2015-3-18	2,457,099.80	19.883	0.0266	19.5225	0.0167	…	…	…	…
2016-1-14	2,457,401.80	19.625	0.0341	19.3705	0.0306	19.229	0.0342	19.475	0.03815

Appendix B
Tables

Table 10
YJH-CSP2 Photometry of SN 2011fh

UT Date	JD	*Y*		*J*		*H*	
		(mag)	(error)	(mag)	(error)	(mag)	(error)
(1)	(2)	(3)	(4)	(5)	(6)	(7)	(8
2013-2-23	2,456,346.86	17.62	0.031	…	…	…	…
2013-2-27	2,456,350.81	17.58	0.03	17.457	0.026	17.19	0.037
2013-3-26	2,456,377.75	17.75	0.023	17.649	0.021	…	…
2015-4-30	2,457,142.58	18.865	0.044	18.833	0.051	18.491	0.0788
2016-3-27	2,457,474.70	18.575	0.075	18.64	0.085	18.25	0.113
2017-5-16	2,457,889.50	18.208	0.043	…	…	…	…

Table 11
Spitzer Photometry of SN 2011fh

UT Date	JD	Channel 1 (3.6 μm)		Channel 2 (4.5 μm)	
		(mag)	(error)	(mag)	(error)
(1)	(2)	(3)	(4)	(5)	(6)
2009-8-6	2,455,050.094	16.019	0.047	15.686	0.045
2009-9-5	2,455,080.09	16.142	0.043	15.77	0.047
2013-3-31	2,456,383.113	15.899	0.045	15.024	0.04
2014-4-4	2,456,752.49	16.27	0.048	15.572	0.04
2014-9-12	2,456,913.073	16.228	0.059	15.492	0.045
2014-10-12	2,456,943.206	16.24	0.052	15.529	0.044
2015-5-16	2,457,158.625	16.265	0.052	15.64	0.045

ORCID iDs

Thallis Pessi https://orcid.org/0000-0001-6540-0767
Jose L. Prieto https://orcid.org/0000-0003-0943-0026
Christopher S. Kochanek https://orcid.org/0000-0001-6017-2961
Ori D. Fox https://orcid.org/0000-0003-2238-1572
Heloise F. Stevance https://orcid.org/0000-0002-0504-4323

References

Adams, S. M., & Kochanek, C. S. 2015, MNRAS, 452, 2195
Abbott, B. P., Abbott, R., Abbott, T. D., et al. 2018, PhRvL, 121, 161101
Adams, S. M., Kochanek, C. S., Prieto, J. L., et al. 2016, MNRAS, 460, 1645
Alonso-García, J., Mateo, M., Sen, B., et al. 2012, AJ, 143, 70
Anderson, J. P., Habergham, S. M., James, P. A., & Hamuy, M. 2012, MNRAS, 424, 1372
Arnett, W. D., Bahcall, J. N., Kirshner, R. P., & Woosley, S. E. 1989, ARA&A, 27, 629
Asari, N. V., Cid Fernandes, R., Stasińska, G., et al. 2007, MNRAS, 381, 263
Asplund, M., Amarsi, A. M., & Grevesse, N. 2021, A&A, 653, A141
Astropy Collaboration, Price-Whelan, A. M., Sipőcz, B. M., et al. 2018, AJ, 156, 123
Astropy Collaboration, Robitaille, T. P., Tollerud, E. J., et al. 2013, A&A, 558, A33
Bacon, R., Vernet, J., Borisova, E., et al. 2014, Msngr, 157, 13
Benetti, S., Chugai, N. N., Utrobin, V. P., et al. 2016, MNRAS, 456, 3296
Berger, E., Soderberg, A. M., Chevalier, R. A., et al. 2009, ApJ, 699, 1850
Bernstein, R., Shectman, S. A., Gunnels, S. M., Mochnacki, S., & Athey, A. E. 2003, Proc. SPIE, 4841, 1694
Bestenlehner, J. M., Crowther, P. A., Caballero-Nieves, S. M., et al. 2020, MNRAS, 499, 1918

Blanton, M. R., & Roweis, S. 2007, AJ, 133, 734
Boian, I., & Groh, J. H. 2018, A&A, 617, A115
Bond, H. E., Bedin, L. R., Bonanos, A. Z., et al. 2009, ApJL, 695, L154
Botticella, M. T., Pastorello, A., Smartt, S. J., et al. 2009, MNRAS, 398, 1041
Bradley, L., Sipöcz, B., Robitaille, T., et al. 2019, astropy/photutils v0.7.2, Zenodo, doi: 10.5281/zenodo.3568287
Brennan, S. J., Fraser, M., Johansson, J., et al. 2021a, arXiv:2102.09572
Brennan, S. J., Fraser, M., Johansson, J., et al. 2021b, arXiv:2102.09576
Cai, Y. Z., Pastorello, A., Fraser, M., et al. 2018, MNRAS, 480, 3424
Cai, Y. Z., Pastorello, A., Fraser, M., et al. 2021, A&A, 654, A157
Castelli, F., & Kurucz, R. L. 2003, in IAU Symp. 201, Modelling of Stellar Atmospheres, ed. N. Piskunov, W. W. Weiss, & D. F. Gray (Cambridge: Cambridge Univ. Press), A20
Chandra, P., Chevalier, R. A., Chugai, N., et al. 2012a, ApJ, 755, 110
Chandra, P., Chevalier, R. A., Irwin, C. M., et al. 2012b, ApJL, 750, L2
Chandra, P., Stockdale, C. J., Chevalier, R. A., et al. 2009, ApJ, 690, 1839
Chugai, N. N. 2001, MNRAS, 326, 1448
Cid Fernandes, R., Mateus, A., Sodré, L., Stasińska, G., & Gomes, J. M. 2005, MNRAS, 358, 363
Dolphin, A. 2016, DOLPHOT: Stellar photometry, Astrophysics Source Code Library, ascl:1608.013
Dopita, M. A., Kewley, L. J., Sutherland, R. S., & Nicholls, D. C. 2016, Ap&SS, 361, 61
Draine, B. T., & Lee, H. M. 1984, ApJ, 285, 89
Drake, A. J., Djorgovski, S. G., Mahabal, A., et al. 2009, ApJ, 696, 870
Eldridge, J. J., Stanway, E. R., Xiao, L., et al. 2017, PASA, 34, e058
Elias-Rosa, N., Benetti, S., Cappellaro, E., et al. 2018, MNRAS, 475, 2614
Elias-Rosa, N., Pastorello, A., Benetti, S., et al. 2016, MNRAS, 463, 3894
Fazio, G. G., Hora, J. L., Allen, L. E., et al. 2004, ApJS, 154, 10
Filippenko, A. V. 1997, ARA&A, 35, 309
Filippenko, A. V. 2000, IAUC, 7421, 3
Foley, R. J., Berger, E., Fox, O., et al. 2011, ApJ, 732, 32
Fox, D. W., Lewin, W. H. G., Fabian, A., et al. 2000, MNRAS, 319, 1154
Fox, O. D., Chevalier, R. A., Dwek, E., et al. 2010, ApJ, 725, 1768
Fox, O. D., Chevalier, R. A., Skrutskie, M. F., et al. 2011, ApJ, 741, 7
Fransson, C., Chevalier, R. A., Filippenko, A. V., et al. 2002, ApJ, 572, 350
Fraser, F. 2020, RSOS, 7, 200467
Fraser, M., Inserra, C., Jerkstrand, A., et al. 2013, MNRAS, 433, 1312
Fraser, M., Kotak, R., Pastorello, A., et al. 2015, MNRAS, 453, 3886
Fraser, M., Stritzinger, M. D., Brennan, S. J., et al. 2021, arXiv:2108.07278
Freedman, W. L. & Carnegie Supernova Project 2005, in ASP Conf. Ser. 339, Observing Dark Energy, ed. S. C. Wolff & T. R. Lauer (San Francisco, CA: ASP), 50
Gal-Yam, A., & Leonard, D. C. 2009, Natur, 458, 865
Gal-Yam, A., Leonard, D. C., Fox, D. B., et al. 2007, ApJ, 656, 372
Gal-Yam, A., Yaron, O., Pastorello, A., et al. 2021, TNSAN, 76, 1
Goranskij, V. P., Barsukova, E. A., Valeev, A. F., et al. 2016, AstBu, 71, 422
Graham, M. L., Bigley, A., Mauerhan, J. C., et al. 2017, MNRAS, 469, 1559
Graham, M. L., Sand, D. J., Valenti, S., et al. 2014, ApJ, 787, 163
Hainich, R., Rühling, U., Todt, H., et al. 2014, A&A, 565, A27
Hamuy, M., Folatelli, G., Morrell, N. I., et al. 2006, PASP, 118, 2
Heger, A., Fryer, C. L., Woosley, S. E., Langer, N., & Hartmann, D. H. 2003, ApJ, 591, 288
Hirai, R., Podsiadlowski, P., Owocki, S. P., Schneider, F. R. N., & Smith, N. 2021, MNRAS, 503, 4276
Ivezic, Z., & Elitzur, M. 1997, MNRAS, 287, 799
Kangas, T., Portinari, L., Mattila, S., et al. 2017, A&A, 597, A92
Kashi, A., Soker, N., & Moskovitz, N. 2013, MNRAS, 436, 2484
Katsuda, S., Maeda, K., Nozawa, T., Pooley, D., & Immler, S. 2014, ApJ, 780, 184
Kennicutt, R. C. J. 1998, ARA&A, 36, 189
Kiewe, M., Gal-Yam, A., Arcavi, I., et al. 2012, ApJ, 744, 10
Kilpatrick, C. D., Foley, R. J., Drout, M. R., et al. 2018, MNRAS, 473, 4805
Kochanek, C. S. 2011, ApJ, 741, 37
Kochanek, C. S., Szczygieł, D. M., & Stanek, K. Z. 2012, ApJ, 758, 142
Kourkchi, E., Courtois, H. M., Graziani, R., et al. 2020, AJ, 159, 67
Krisciunas, K., Contreras, C., Burns, C. R., et al. 2017, AJ, 154, 211
Kuncarayakti, H., Anderson, J. P., Galbany, L., et al. 2018, A&A, 613, A35
Langer, N. 2012, ARA&A, 50, 107
Leonard, D. C., Filippenko, A. V., Barth, A. J., & Matheson, T. 2000, ApJ, 536, 239
Levesque, E. M., Berger, E., Kewley, L. J., & Bagley, M. M. 2010, AJ, 139, 694
Levesque, E. M., Stringfellow, G. S., Ginsburg, A. G., Bally, J., & Keeney, B. A. 2014, AJ, 147, 23
Margutti, R., Milisavljevic, D., Soderberg, A. M., et al. 2014, ApJ, 780, 21
Mateus, A., Sodré, L., Cid Fernandes, R., et al. 2006, MNRAS, 370, 721
Mathis, J. S., Rumpl, W., & Nordsieck, K. H. 1977, ApJ, 217, 425
Mauerhan, J., Williams, G. G., Smith, N., et al. 2014, MNRAS, 442, 1166
Mauerhan, J. C., Smith, N., Filippenko, A. V., et al. 2013, MNRAS, 430, 1801
Maza, J., Hamuy, M., Antezana, R., et al. 2009, CBET, 1928, 1
Monard, L. A. G., Prieto, J. L., & Seth, K. 2011, CBET, 2799, 1
Moriya, T., Tominaga, N., Tanaka, M., et al. 2010, ApJ, 719, 1445
Moriya, T. J. 2015, ApJL, 803, L26
Nicholl, M. 2018, RNAAS, 2, 230
Nyholm, A., Sollerman, J., Tartaglia, L., et al. 2020, A&A, 637, A73
Ofek, E. O., Sullivan, M., Cenko, S. B., et al. 2013, Natur, 494, 65
Ofek, E. O., Sullivan, M., Shaviv, N. J., et al. 2014, ApJ, 789, 104
Pastorello, A., Botticella, M. T., Trundle, C., et al. 2010, MNRAS, 408, 181
Pastorello, A., Cappellaro, E., Inserra, C., et al. 2013, ApJ, 767, 1
Pastorello, A., Kochanek, C. S., Fraser, M., et al. 2017, MNRAS, 474, 197
Pastorello, A., Mason, E., Taubenberger, S., et al. 2019a, A&A, 630, A75
Pastorello, A., Mattila, S., Zampieri, L., et al. 2008, MNRAS, 389, 113
Pastorello, A., Pumo, M. L., Navasardyan, H., et al. 2012, A&A, 537, A141
Pastorello, A., Reguitti, A., Morales-Garoffolo, A., et al. 2019b, A&A, 628, A93
Pastorello, A., Smartt, S. J., Mattila, S., et al. 2007, Natur, 447, 829
Paturel, G., Theureau, G., Bottinelli, L., et al. 2003, A&A, 412, 57
Paxton, B., Bildsten, L., Dotter, A., et al. 2011, ApJS, 192, 3
Paxton, B., Cantiello, M., Arras, P., et al. 2013, ApJS, 208, 4
Paxton, B., Marchant, P., Schwab, J., et al. 2015, ApJS, 220, 15
Paxton, B., Schwab, J., Bauer, E. B., et al. 2018, ApJS, 234, 34
Phillips, M. M., Contreras, C., Hsiao, E. Y., et al. 2019, PASP, 131, 014001
Pooley, D., Lewin, W. H. G., Fox, D. W., et al. 2002, ApJ, 572, 932
Prieto, J. L., Brimacombe, J., Drake, A. J., & Howerton, S. 2013, ApJL, 763, L27
Prieto, J. L., Kistler, M. D., Thompson, T. A., et al. 2008, ApJL, 681, L9
Prieto, J. L., Rest, A., Bianco, F. B., et al. 2014, ApJL, 787, L8
Prieto, J. L., & Seth, K. 2011, CBET, 2799, 2
Quataert, E., Fernández, R., Kasen, D., Klion, H., & Paxton, B. 2016, MNRAS, 458, 1214
Quataert, E., & Shiode, J. 2012, MNRAS, 423, L92
Ransome, C. L., Habergham-Mawson, S. M., Darnley, M. J., et al. 2021, MNRAS, 506, 4715
Reguitti, A., Pastorello, A., Pignata, G., et al. 2019, MNRAS, 482, 2750
Rest, A., Prieto, J. L., Walborn, N. R., et al. 2012, Natur, 482, 375
Sana, H., de Mink, S. E., de Koter, A., et al. 2012, Sci, 337, 444
Schechter, P. L., Mateo, M., & Saha, A. 1993, PASP, 105, 1342
Schlafly, E. F., & Finkbeiner, D. P. 2011, ApJ, 737, 103
Schlegel, E. M. 1990, MNRAS, 244, 269
Shiode, J. H., & Quataert, E. 2014, ApJ, 780, 96
Simcoe, R. A., Burgasser, A. J., Schechter, P. L., et al. 2013, PASP, 125, 270
Smith, N. 2006, ApJ, 644, 1151
Smith, N. 2013, MNRAS, 429, 2366
Smith, N. 2014, ARA&A, 52, 487
Smith, N. 2017, in Handbook of Supernovae, ed. A. W. Alsabti & P. Murdin (Berlin: Springer), 403
Smith, N., Andrews, J. E., & Mauerhan, J. C. 2016a, MNRAS, 463, 2904
Smith, N., Andrews, J. E., Mauerhan, J. C., et al. 2016b, MNRAS, 455, 3546
Smith, N., Andrews, J. E., Rest, A., et al. 2018a, MNRAS, 480, 1466
Smith, N., & Arnett, W. D. 2014, ApJ, 785, 82
Smith, N., & Frew, D. J. 2011, MNRAS, 415, 2009
Smith, N., Ganeshalingam, M., Chornock, R., et al. 2009, ApJL, 697, L49
Smith, N., Gehrz, R. D., Hinz, P. M., et al. 2003, AJ, 125, 1458
Smith, N., Li, W., Silverman, J. M., Ganeshalingam, M., & Filippenko, A. V. 2011, MNRAS, 415, 773
Smith, N., Mauerhan, J. C., Kasliwal, M. M., & Burgasser, A. J. 2013, MNRAS, 434, 2721
Smith, N., Mauerhan, J. C., & Prieto, J. L. 2014, MNRAS, 438, 1191
Smith, N., Miller, A., Li, W., et al. 2010, AJ, 139, 1451
Smith, N., Rest, A., Andrews, J. E., et al. 2018b, MNRAS, 480, 1457
Stanway, E. R., & Eldridge, J. J. 2018, MNRAS, 479, 75
Stevance, H., Eldridge, J., & Stanway, E. 2020a, JOSS, 5, 1987
Stevance, H. F., Eldridge, J. J., McLeod, A., Stanway, E. R., & Chrimes, A. A. 2020b, MNRAS, 498, 1347
Stritzinger, M. D., Taddia, F., Fraser, M., et al. 2020, A&A, 639, A103
Strotjohann, N. L., Ofek, E. O., Gal-Yam, A., et al. 2021, ApJ, 907, 99
Sukhbold, T., Ertl, T., Woosley, S. E., Brown, J. M., & Janka, H. T. 2016, ApJ, 821, 38
Szalai, T., Fox, O. D., Arendt, R. G., et al. 2021, ApJ, 919, 17
Szalai, T., Zsíros, S., Fox, O. D., Pejcha, O., & Müller, T. 2019, ApJS, 241, 38
Taddia, F., Sollerman, J., Fremling, C., et al. 2015, A&A, 580, A131
Taddia, F., Stritzinger, M. D., Sollerman, J., et al. 2013, A&A, 555, A10

Tartaglia, L., Pastorello, A., Sullivan, M., et al. 2016, MNRAS, 459, 1039
Thoene, C., de Ugarte Postigo, A., Leloudas, G., Cano, Z., & Maeda, K. 2015, ATel, 8417, 1
Thompson, T. A., Prieto, J. L., Stanek, K. Z., et al. 2009, ApJ, 705, 1364
Thöne, C. C., de Ugarte Postigo, A., Leloudas, G., et al. 2017, A&A, 599, A129
Tody, D. 1986, Proc. SPIE, 627, 733
Tody, D. 1993, in ASP Conf. Ser. 52, Astronomical Data Analysis Software and Systems II, ed. R. J. Hanisch, R. J. V. Brissenden, & J. Barnes (San Francisco, CA: ASP), 173
Van Dyk, S. D., Peng, C. Y., King, J. Y., et al. 2000, PASP, 112, 1532
van Dyk, S. D., Weiler, K. W., Sramek, R. A., & Panagia, N. 1993, ApJL, 419, L69
Wagner, R. M., Vrba, F. J., Henden, A. A., et al. 2004, PASP, 116, 326
Williams, B. F., Lang, D., Dalcanton, J. J., et al. 2014, ApJS, 215, 9
Williams, C. L., Panagia, N., Van Dyk, S. D., et al. 2002, ApJ, 581, 396
Woosley, S. E., Blinnikov, S., & Heger, A. 2007, Natur, 450, 390
Yaron, O., & Gal-Yam, A. 2012, PASP, 124, 668